TITLE: Using bottom trawls to monitor subsurface water clarity in marine ecosystems

AUTHORS:
Sean K. Rohan[1,2,*]
Stan Kotwicki[1]
Kelly A. Kearney[3,1]
Jennifer A. Schulien[4]
Edward A. Laman[1]
Edward D. Cokelet[5]
David A. Beauchamp[6]
Lyle L. Britt[1]
Kerim Y. Aydin[1]
Stephani G. Zador[1]

AFFILIATIONS AND ADDRESSES:
[1]–National Marine Fisheries Service, Alaska Fisheries Science Center, National Oceanic and Atmospheric Administration, 7600 Sand Point Way NE, Seattle, WA 98115, USA.

[2]–University of Washington, School of Aquatic and Fishery Sciences, Box 355020, Seattle, WA 98195, USA.

[3]–University of Washington, Joint Institute for the Study of the Atmosphere and Oceans, Seattle, WA, USA

[4]–U.S. Geological Survey, Western Ecological Research Center, Santa Cruz Field Office, 2882 Mission St., Santa Cruz, CA 95060, USA.

[5]–Pacific Marine Environmental Laboratory, National Oceanic and Atmospheric Administration, 7600 Sand Point Way NE, Seattle, WA 98115, USA.

[6]–U.S. Geological Survey, Western Fisheries Research Center, 6505 NE 65th Street, Seattle, Washington 98115, USA.

CORRESPONDING AUTHOR:
[*]–sean.rohan@noaa.gov, tel: 206-526-4121

ABSTRACT

Biophysical processes that affect subsurface water clarity play a key role in ecosystem function. However, subsurface water clarity is poorly monitored in marine ecosystems because doing so requires in-situ sampling that is logistically difficult to conduct and sustain. Novel solutions are thus needed to improve monitoring of subsurface water clarity. To that end, we developed a sampling method and data processing algorithm that enable the use of bottom trawl fishing gear as a platform for conducting subsurface water clarity monitoring using trawl-mounted irradiance sensors without disruption to fishing operations. The algorithm applies quality control checks to irradiance measurements and calculates the downwelling diffuse attenuation coefficient, K_d, and optical depth, ζ– apparent optical properties (AOPs) that characterize the rate of decrease in downwelling irradiance and relative irradiance transmission to depth, respectively. We applied our algorithm to irradiance measurements, obtained using bottom-trawl-mounted archival tags equipped with a photodiode collected during NOAA's Alaska Fisheries Science Center annual summer bottom trawl surveys of the eastern Bering Sea continental shelf from 2004 to 2018. We validated our AOPs by quantitatively comparing surface-weighted K_d from tags to the multi-sensor $K_d(490)$ product from the Ocean Colour Climate Change Initiative project (OC-CCI) and qualitatively evaluating whether tag K_d was consistent with patterns of subsurface chlorophyll-a concentrations predicted by a coupled regional physical-biological model (Bering10K-BESTNPZ). We additionally examined patterns and trends in water clarity in the eastern Bering Sea. Key findings are: 1) water clarity decreased significantly from 2004 to 2018; 2) a recurrent, pycnocline-associated, maximum in K_d occurred over much of the northwestern shelf, putatively due to a subsurface chlorophyll maximum; and

3) a turbid bottom layer (nepheloid layer) was present over a large portion of the eastern Bering Sea shelf. Our study demonstrates that bottom trawls can provide a useful platform for monitoring water clarity, especially when trawling is conducted as part of a systematic stock assessment survey.

KEYWORDS: apparent optical properties, bottom trawl survey, eastern Bering Sea, nepheloid layer, regional ocean modeling system, remote sensing, subsurface chlorophyll maximum, archival tag, downwelling diffuse attenuation coefficient, optical depth

1. INTRODUCTION

Water clarity regulates heat transfer and mediates rates of primary production that set the baseline for total ecosystem production and food chain efficiency (Dickman et al., 2008; Kirk, 2011; Opdal et al., 2019). Water clarity also affects visual processes, so changes in water clarity can shift the balance of competition among animals with different visual capabilities, sensory modes of foraging, and vulnerability to visual predation (Aksnes et al., 2004; Eiane et al., 1997). Consequently, changes in water clarity can provide useful insights into ecosystem change.

Near-surface water clarity has changed over multiple decades in many marine regions, providing information on how changes in water clarity are associated with changes in the structure and function of marine ecosystems (Aksnes, 2007; Aksnes and Ohman, 2009; Capuzzo et al., 2015; Haraldsson et al., 2012). These insights result from systematic monitoring of near-surface water clarity conducted since the invention of the Secchi disk in 1865 (Pitarch, 2020). In recent decades, satellite-based remote sensing has vastly improved the capacity to monitor near-surface water clarity under clear-sky conditions, at a global extent, with increasingly fine spatial and temporal resolution. By combining data sets from multiple sampling methods (*e.g.*, Secchi disk, Forel-Ule color comparator, satellite based passive remote sensing), many marine systems have time-series that inform how near-surface water clarity has changed over multiple decades, affecting ecological processes across multiple spatial, temporal, and organizational scales (Aksnes and Ohman, 2009; Capuzzo et al., 2015; Dupont and Aksnes, 2013; Sandén and Håkansson, 1996; Tolvanen et al., 2013; Wernand et al., 2013; Boyce et al., 2014).

In contrast to extensive near-surface monitoring, subsurface water clarity remains poorly characterized due to the logistical difficulties of sampling. Despite near global coverage, passive satellite-based remote sensing only characterizes near-surface water clarity down to first optical depth (*i.e.*, depth of 10% downwelling diffuse irradiance). Subsurface monitoring requires in situ sampling from crewed vessels, fixed moorings, or mobile samplers such as Biogeochemical-Argo floats and autonomous underwater vehicles (Bittig et al., 2019; Brown et al., 2004; Mitchell et al., 2018). While autonomous mobile samplers have continually improved (Hemsley et al., 2015; Mitchell et al., 2018), they have not achieved ubiquitous coverage due to cost, relatively slow speed, currents, and potential for interference with vessel traffic.

Despite generally limited monitoring, it is clear that changes in subsurface water clarity are indicative of ecosystem change. Subsurface algal blooms generate subsurface chlorophyll maximum layers that contribute substantially to total productivity in many marine systems (Cullen, 2015). Changes in the timing or intensity of subsurface blooms would therefore be expected to alter subsurface water clarity. In addition, currents drive the resuspension of seafloor sediments (organic and inorganic), producing nepheloid layers that may play an important role in nutrient cycling, benthic suspension and filter feeding, and animal distribution and behavior (Jumars et al., 2015; McCave, 2019; Riisgård and Larsen, 2015). Subsurface chlorophyll maximum layers and nepheloid layers occur too deep to be monitored using passive satellite-based remote sensing (Barbieux et al., 2019; Hostetler et al., 2018; Schulien et al., 2017).

One option to improve subsurface monitoring is to deploy optical sampling equipment on existing platforms that are not explicitly designed to collect optical data. For example, attenuation coefficients derived from irradiance measurements collected using light-sensitive archival tags attached to pinnipeds and large pelagic fishes are used to make reasonably accurate predictions of chlorophyll-a concentration in the mixed layer (Jaud et al., 2012; O'Toole et al., 2017, 2014) and at fine-scale vertical resolution within the water column (Bayle et al., 2015;

Nowak, 2019; Teo et al., 2009). However, unconventional sampling platforms can make it challenging to obtain measurements that are accurate, precise, reproducible and comparable to conventional data.

Given their regular frequency of sampling, standardized approach to data collection, and often large spatial coverage, fisheries-independent bottom trawl surveys are an appealing platform for water clarity monitoring. Already, physical ocean data collected during bottom trawl surveys have been used to characterize ocean circulation patterns and the fine-scale thermohaline structure of the water column (Cokelet, 2016). These data have also been used as covariates in species distribution models that have improved understanding of habitat requirements of marine fauna (Laman et al., 2018, 2014; Rooper et al., 2019). The addition of water clarity information will likely improve understanding of species-environment relationships because the intensity and spectrum of environmental light affect the sensory capabilities of aquatic animals (Britt et al., 2001; Caves et al., 2017; Lythgoe, 1972; Schweikert et al., 2018). Further, combining water clarity monitoring with biogeochemical sampling would facilitate the development of bio-optical models that may be used to estimate the composition of optically active constituents of the water column (*e.g.*, chlorophyll-a, chromophoric dissolved organic matter [CDOM]).

In this study, we derived apparent optical properties (AOPs), the downwelling diffuse attenuation coefficient (K_d) and optical depth (ζ), from bottom-trawl-mounted light-sensitive archival tags to evaluate the utility of bottom trawl surveys as a platform for monitoring surface and subsurface water clarity. Our study region was the eastern Bering Sea, a subarctic semi-enclosed sea with an expansive shelf where summer bottom trawl surveys have been conducted annually since 1982 and water column light data have been collected annually since 2004. To validate trawl-derived AOPs, we 1) quantitatively evaluate if near-surface tag-based attenuation coefficients are consistent with attenuation coefficients derived from satellite-based measurements of ocean color, and 2) qualitatively evaluate whether the patterns in AOPs are consistent with predictions from a coupled physical-biological model of primary production. We describe patterns of variation in AOPs in the eastern Bering Sea during summer 2004–2018 and synthesize our findings with the current understanding of physical and biological processes that drive variation in water clarity in the eastern Bering Sea. Finally, we provide recommendations for how sampling during bottom trawl surveys can be extended to improve monitoring of water clarity.

2. REGIONAL SETTING

The eastern Bering Sea is a highly productive subarctic coastal ecosystem that supports several of the world's largest commercial fisheries along with large populations of marine mammals and seabirds. The broad continental shelf of the eastern Bering Sea slopes gently from the Alaska mainland to the continental shelf break at ~180 m (Fig. 1). Factors that influence water clarity in the eastern Bering Sea are: surface and subsurface phytoplankton, chromophoric dissolved organic matter (CDOM) and sediment originating from rivers, and resuspension of seafloor sediment driven by currents, winds, and tides (*i.e.*, nepheloid layers). The relative importance of these factors varies over space and time due to physical and biogeochemical processes.

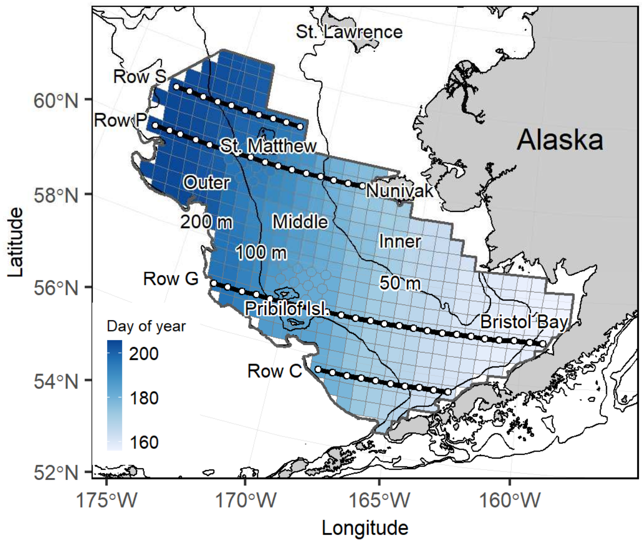

Figure 1. Eastern Bering Sea bottom trawl survey area, showing the average sampling day of year during 2004–2018 for each of the 376 survey grid stations. Thick black lines and white points denote the location of shelf-wide cross-sections and stations highlighted in analyses of the vertical structure of the water column. Inner (0–50 m bottom depth), middle (50–100 m), and outer (100–180 m) domains are shown.

During summer, the eastern Bering Sea continental shelf is generally divided into three biophysical domains: the inner domain (0–50 m bottom depth), middle domain (50–100 m), and outer domain (100–180 m) (Coachman, 1986). The inner and middle domains are divided by an inner front that occurs roughly along the 50 m isobath. The middle and outer shelf domains are divided by a front that occurs roughly along the 100 m isobath. The domains have differences in biological processes, physical processes, and water column structure. The inner domain has relatively low salinity and features a fully-mixed or weakly stratified water column maintained by wind and tidal mixing (Coachman, 1986; Kachel et al., 2002; Ladd and Stabeno, 2012). North of Nunivak Island (~62°N), the inner front is located inshore of the 50 m isobath due to weaker tidal mixing and alongshore northward advection of freshwater input from rivers (Danielson et al., 2011; Ladd and Stabeno, 2012; Mordy et al., 2017). South of ~57°N, the inner domain can extend offshore to depths of ~70 m (Cokelet, 2016). The middle domain features a stratified two-layer water column with a sharp pycnocline. The density structure over the middle domain is maintained by wind mixing of the surface layer and tidal mixing of the bottom layer (Coachman, 1986; Stabeno et al., 2012a). The outer domain is characterized by a wind-mixed surface layer and a tidally mixed bottom layer with a gradual density transition between the two domains. Summertime geostrophic current velocities are slow, averaging 0–2 cm s^{-1} over most of the eastern Bering Sea shelf, with a net northward transport through Bering Strait (Cokelet, 2016). Stronger flow is observed along the 50 m and 100 m isobaths, which accounts for 50% of transport through Bering Strait (Stabeno et al., 2016).

The extent of seasonal sea-ice and timing of sea-ice melt sets up the summer thermohaline structure of the eastern Bering Sea. Interannual variation in wind velocity, air temperature, and water temperature drive variation in winter sea-ice extent (Stabeno et al., 2017). Since the 1970s, at maximum, seasonal sea ice has extended to the Alaska Peninsula (most recently in 2012), while at its minimum in 2018, the ice edge was north of St. Matthew Island (Stabeno and Bell, 2019). As sea-ice melts in the spring–summer, it cools and freshens the water column and causes the formation of a cold pool (bottom temperature <2° C) over the middle and outer shelf. Thus, the cold pool is considered a remnant of winter sea ice. When ice melts in early spring, strong winds mix the water column and stratification is delayed until the water column begins to warm (Ladd and Stabeno, 2012). When sea-ice melts later, the abatement of winter storms leads to weaker wind-mixing, allowing meltwater to form a low salinity surface layer that contributes to stratification (Cokelet, 2016; Ladd and Stabeno, 2012; Stabeno et al., 2012a). Further north where sea-ice persists longer, freshening from ice melt and temperature contribute to stratification (Ladd and Stabeno, 2012).

The timing of sea-ice melt affects the spring phytoplankton bloom timing in the mixed layer. When sea-ice persists until mid-March, a spring bloom of ice-associated phytoplankton occurs at the surface as the sea-ice thins and melts (Hunt et al., 2011; Sigler et al., 2014). When ice melts earlier than mid-March, the spring bloom is delayed and concurrent with the onset of thermal stratification. The spring bloom produces a surface chlorophyll maximum and causes rapid depletion of nutrients in the mixed layer (Mordy et al., 2012). During summer, primary production is nutrient-limited in the mixed layer because strong stratification inhibits vertical infusion of nutrients from the nutrient-rich bottom layer of the middle and outer domain. However, energetic storms can deepen the mixed layer and replenish nutrients to produce a phytoplankton bloom that peaks 1–2 weeks after the storm (Sambrotto et al., 1986; Stabeno et al., 2010).

Spatiotemporal variation in nutrient cycling and replenishment causes variation in primary production dynamics across the eastern Bering Sea. In the bottom layer over the northern middle and outer domain, nitrate concentrations are relatively high, and are sufficient to sustain production throughout the summer if enough light penetrates into the pycnocline (Stabeno et al., 2019). This production leads to the formation of a pycnocline-associated subsurface chlorophyll maximum layer that can persist through summer (Stabeno et al., 2012a, 2012b). Summer observations of the subsurface layer are sporadic because there is no regular in-situ monitoring. However, coupled bio-physical models predict the spatiotemporal dynamics of the layer (Kearney et al., 2020). Towards the inner domain, nitrate concentrations decrease due to limited onshore advection of bottom water. As such, primary production in the inner domain is mainly the result of regenerative production (*i.e.*, production supported by the reuptake of excreted ammonia; Mordy et al., 2017).

Numerous rivers discharge from the Alaska mainland into the eastern Bering Sea, supplying freshwater rich with CDOM and suspended sediment. These optically unique water sources affect water clarity over the eastern Bering Sea shelf (Naik et al., 2013). From October–May, strong winds and weak cross-shelf density gradients allow advection of fluvial water sources over the middle and outer shelf (Danielson et al., 2011). During spring and summer, river discharge is predominantly advected northward alongshore of mainland Alaska by the Alaska Coastal Current; minimal offshore advection occurs due to a strong cross-shelf density gradient and weak offshore wind (Danielson et al., 2011).

There is a bottom-associated nepheloid layer over parts of the eastern Bering Sea shelf, although variation in the nepheloid layer and processes that cause its formation are poorly characterized due to a lack of monitoring (Feely et al., 1981; Kawana, 1975; McManus and Smyth, 1970). Generally, nepheloid layers are caused by resuspension of seafloor sediment by currents generated by wind, tides, geostrophic circulation, internal waves, benthic storms, and eddies (McCave, 2019). The structure of a nepheloid layer depends on current velocities, sediment composition, settling rates of particulates, and the density structure of the water column.

Although changes in the subsurface environment have been poorly characterized, changes in light transmission dynamics through the upper water column are both a cause and consequence of ecosystem changes in the eastern Bering Sea. Near-surface waters of the eastern Bering Sea became bluer from 1935 to 1998, which suggests changes in the ecosystem caused a decrease in near-surface chlorophyll concentrations (Wernand et al., 2013). In recent warm years with low sea-ice extent (2014–2016), findings suggest chlorophyll and net primary production have increased relative to recent cold years (2007–2011) (Lomas et al., 2020). Since 1997, large-scale blooms of the coccolithophore *Emiliania huxleyi* have become common in the fall (August–September) despite being absent from the stratigraphic sediment record in preceding decades (Harada et al., 2012; Iida et al., 2012; Ladd et al., 2018). This change is thought to be the result of a climate-mediated shift in the thermohaline structure of the water column and nutrient that favors the growth of *E. huxleyi* and may affect zooplankton grazing (Olson and Strom, 2002) and foraging efficiency for visually foraging predators (Lovvorn et al., 2001). Finally, it has been suggested that reduction of seasonal sea-ice due to climate change will increase the productivity of pelagic fish stocks in the eastern Bering Sea by enhancing visual foraging opportunity (Langbehn and Varpe, 2017).

3. METHODS

3.1 Data sources and processing

3.1.1 Bottom trawl irradiance data

Irradiance, temperature, and salinity data were collected during annual summer (early June–early August) bottom trawl surveys of the eastern Bering Sea continental shelf conducted by the Resource Assessment and Conservation Engineering Division of NOAA's Alaska Fisheries Science Center. Each year, the bottom trawl survey sampled the same 376 survey stations arranged on a regularly-spaced 20×20 nmi (37×37 km) grid, with 'corner stations' in some areas (Fig. 1). Sampling was generally conducted near the center of survey grid cells at approximately the same bottom depth every year. Bottom depths sampled by the survey ranged from ~20 m along the Alaska mainland to ~180 m along the continental shelf break. Two vessels were used to conduct surveys each year, with each vessel sampling approximately half of the stations. Surveys progressed from interior Bristol Bay in the southeast to the outer continental shelf in the northwest. Bottom trawl sampling started no earlier than 30 minutes after sunrise and ended no later than 30 minutes before sunset (Stauffer, 2004).

Bottom trawl surveys collected environmental data using sensors (described below) attached to the outside of the top panel of the bottom trawl gear (83-112 Eastern trawl). The sensors were positioned 0.5–2.0 m aft of the headrope of the trawl gear. When deployed in fishing configuration, the headrope of the bottom trawl gear was ~2.5 m above the seafloor. Thus, sensors collected data from the sea surface to ~2.5 m above the seafloor during each trawl deployment (downcast) and retrieval (upcast). Tows were conducted at a target vessel speed of 2.8–3.2 knots (1.44–1.65 m s^{-1}) for 30 minutes, typically resulting in upcasts and downcasts ~1.5 nmi (2.8 km) apart. Vessels were underway during trawl deployment and retrieval, so upcasts and downcasts were oblique profiles of the water column.

From 2004 to 2018, irradiance measurements were collected using archival tags equipped with a blue-filtered photodiode (Wildlife Computers TDR-Mk9). Photodiodes are rugged, energy efficient, have a relatively stable response, and are simple to calibrate, but are less sensitive than specialized detectors (Mobley, 1994). Archival tags were used because they are relatively inexpensive, have a low-profile that minimizes drag on trawl gear, and can withstand rough treatment during deployment. Archival tags were affixed to a triangular, white polyurethane base plate assembly with shackles at the forward corners (Fig. 2). During bottom trawl survey hauls, archival tag assemblies were shackled to the trawl gear with the photoelectric cell facing upward to approximate downwelling irradiance. Shading of the archival tag was not a concern because the trawl gear was >50 m behind vessels during casts and vessel wake was negligible. From 2006 to 2018, a deck-mounted archival tag was deployed in an unobstructed location atop of the wheelhouse of each survey vessel, providing surface irradiance measurements. Trawl-mounted archival tags sampled at a rate of 1 Hz, while deck-mounted archival tags sampled at 0.1 Hz. Depths for archival tag irradiance measurements were obtained from a Seabird SBE-39 temperature depth recorder with an internal clock synchronized to the archival tag internal clock to increase measurement precision and mitigate bias in archival tag depth measurements (Rohan et al., 2020).

Figure 2. Archival tag affixed to polyurethane base plate assembly with shackles at the forward corners.

The archival tags used an onboard conversion to record irradiance measurements in relative units that had a maximum integer range of 25–225, corresponding with intensities from 10×10^{-12} W cm^{-2} to 5×10^{-2} W cm^{-2}. A blue filter on the photoelectric cell causes the archival tag to have a peak spectral sensitivity at 465 nm, with a 50% response bandwidth of 420–470 nm (Vacquié-Garcia et al., 2017). The tags have some sensitivity extending to shorter (ultraviolet A) and longer wavelengths (green–red), as detailed by Rohan et al. (2020). Herein, we symbolically represent the spectral band of the tag as λ_{tag}.

Archival tag measurements are not direct analogues of measurements from conventional radiant energy detectors because they are not designed to measure radiant energy with a specific geometry (*e.g.* radiance, planar irradiance, diffuse irradiance). Measurements from TDR-Mk10[1] archival tags are irradiances that geometrically fall between radiance and planar irradiance. The peak response of the sensor occurs when the main axis of the incident radiance field is perpendicular to the plane of the sensor (*i.e.* 90° zenith angle) and decreases at lower incident angles (Vacquié-Garcia et al., 2017). Yet at low angles, the drop-off in the response is more extreme than for a cosine corrected planar irradiance detector (Vacquié-Garcia et al., 2017). Despite their unconventional geometry, archival tag irradiance measurements can be used to derive attenuation coefficients that closely approximate the downwelling planar attenuation coefficient from conventional detectors (Nowak, 2019). Further, archival tag irradiance measurements have been used to calculate vertical attenuation coefficients that allow reasonably accurate predictions of chlorophyll-a concentrations in marine systems (Bayle et al., 2015; Jaud et al., 2012; O'Toole et al., 2017, 2014; Teo et al., 2009). Thus, archival tags can be used to indirectly characterize bio-optical properties.

3.1.2 Irradiance data processing

We developed an algorithm to quality control bottom trawl irradiance data and calculate two apparent optical properties (AOPs): optical depth, $\zeta(z, \lambda)$, and the downwelling diffuse attenuation coefficient, $K_d(z, \lambda)$ m^{-1}. Optical depth, $\zeta(z, \lambda)$, is a dimensionless ratio that characterizes the proportion of downwelling irradiance of wavelength λ just beneath the sea

[1] Light sensor components on TDR-Mk10 archival tags are identical to components on TDR-Mk9 archival tags (Hamamatsu S2387 photodiode, blue spectral bandpass filter, epoxy casing with a refractive index of 1.56).

surface that reaches depth z (m). The downwelling diffuse attenuation coefficient, $K_d(z, \lambda)$ m^{-1}, characterizes the rate of decrease of the natural logarithm of the downwelling irradiance of wavelength λ at depth z.

Initial phases of the design, application, and evaluation of the algorithm are described in Rohan et al. (2020), who found the algorithm generated reproducible and precise values of $\zeta(z, \lambda_{tag})$ and $K_d(z, \lambda_{tag})$ in the eastern Bering Sea. Here, we build on this research by additionally evaluating whether $\zeta(z, \lambda_{tag})$ and $K_d(z, \lambda_{tag})$ are consistent with optical properties obtained using established sampling and data processing methods and applying these optical metrics to evaluate changes in water clarity in the eastern Bering Sea. Below, we summarize the design of the algorithm and underlying rationale.

The algorithm first converts archival tag irradiance measurements units to radiometric units based on a blue-spectrum conversion equation reported by the tag manufacturer:

$$yz{=}z10^{(x-2z \quad /2z},z \qquad (1z$$

where y is irradiance in W cm^{-2}, and x is the integer measurement recorded by the tag. Under constant irradiance, archival tag measurements vary by two integer units (absolute precision) and, for a given irradiance level, individual tags differ by approximately two integer units (Kotwicki et al., 2009; Vacquié-Garcia et al., 2017). Nevertheless, $\zeta(Z, \lambda_{tag})$ and $K_d(Z, \lambda_{tag})$ are calculated using relative changes in irradiance so the absolute range of individual tags is irrelevant so long as tags have a proportionally equal response to changes in downwelling planar irradiance and values are within the absolute sensitivity range of the tags.

Next, the algorithm calculates the geometric mean irradiance for 2-m depth bins for every cast. The depth interval for binning (2-m) and use of a geometric mean were chosen based on trial-and-error to minimize near-surface fluctuations that were likely caused by wave-induced refraction and potentially unstable orientation of the archival tag near the surface.

Filters are often used to distinguish signal from noise in irradiance measurement cast data (*e.g.* Smith and Baker, 1984) but conventional filter methods (*e.g.* Kalman filter) were unsuitable for bottom trawl survey irradiance profiles because they retained data from casts where irradiance measurements fluctuated abruptly due to probable sampling artifacts (e.g. successive order-of-magnitude increases and decreases in irradiance). The abrupt shifts may have occurred due to obstruction of the tag or a change in the orientation of the tag. To address this issue, the algorithm uses a stepwise point removal filter to remove shallower irradiances that are lower (darker) than irradiances deeper in the water column, based on the expectation that irradiance should decrease as depth increases. For example, the stepwise filter omits $E_d(1, \lambda_{tag})$ if $E_d(1, \lambda_{tag}) < E_d(3, \lambda_{tag})$. The stepwise filter removes points until the following condition is satisfied:

$$E_d(z_1, \lambda_{tag}) \geq E_d(z_2, \lambda_{tag}) \geq \cdots \geq E_d(z_{max}, \lambda_{tag})$$

where $E_d(z_i, \lambda_{tag})$ are downwelling irradiance values ordered by depth. Casts where data are missing or omitted from three consecutive depth bins are flagged and excluded from subsequent processing.

The archival tag photodiode should be facing upward in order to calculate AOPs that approximate those based on diffuse downwelling irradiance. Thus, the algorithm employs quality control checks to detect and exclude casts with improper orientation (Rohan et al. [2020]; Supplementary Material: *Detecting archival tag orientation errors*).

Irradiance measurements from the 1-m depth bin are missing or excluded during quality control checks for some casts, which prevents subsequent calculation of $\zeta(z, \lambda_{tag})$. Therefore, the algorithm uses a linear extrapolation to estimate irradiance for the 1-m depth bin when missing.

The extrapolation method explains 96% of the variation in log-transformed irradiance for the 1-m depth bin (Rohan et al., 2020).

The algorithm is used to calculate optical depth $\zeta(z, \lambda_{tag})$, and the diffuse irradiance attenuation coefficient, $K_d(z, \lambda_{tag})$, from casts that pass quality control checks. From the Beer-Lambert equation, downwelling irradiance at depth z, $E_d(z, \lambda)$, is approximately related to downwelling irradiance just below the surface, $E_d(0^-, \lambda)$, as:

$$E_d(z, \lambda) = E_d(0^-, \lambda)\, e^{-K_d(0^- \to z, \lambda) z}, \quad (2)$$

where $K_d(0^- \to z, \lambda)$ (m^{-1}) is the downwelling diffuse attenuation coefficient between just below the sea surface and depth Z (Gordon, 1989). Optical depth, $\zeta(z,\lambda)$, is the product of depth and $K_d(0^- \to z, \lambda)$:

$$\zeta(z, \lambda) = K_d(0^- \to z, \lambda)\, z = \ln\left(E_d(0^-, \lambda)\right) - \ln\left(E_d(z, \lambda)\right). \quad (3)$$

Larger values of $\zeta(z,\lambda)$ correspond with darker conditions.

Because $E_d(1)$ is the shallowest value for each cast, the algorithm calculates $\zeta(z, \lambda_{tag})$ as:

$$\zeta(z, \lambda_{tag}) = \ln\left(E_d(1, \lambda_{tag})\right) - \ln\left(E_d(z, \lambda_{tag})\right). \quad (4)$$

Through an infinitesimally thin slice of water at depth z, the downwelling diffuse attenuation coefficient, $K_d(z, \lambda)$, is defined as:

$$K_d(z, \lambda) = -\frac{1}{E_d(z, \lambda)} \frac{dE_d(z, \lambda)}{dz}. \quad (5)$$

In natural waters, $K_d(z, \lambda)$ varies with depth due to variation in optically active constituents (e.g. chlorophyll-a, CDOM). Because in-situ radiometric measurements alone do not provide a basis to analytically calculate $K_d(z, \lambda)$, a numerical approximation is typically used to estimate $K_d(z, \lambda)$. Our approach to numerical approximation of $K_d(z, \lambda_{tag})$ is described in the Supplementary Material (*Numerical approximation of $K_d(z, \lambda_{tag})$*) and Rohan et al. (2020).

We used $\zeta(z, \lambda_{tag})$ to estimate the following proxies of near-surface water clarity: the depths where irradiance was reduced to 10% ($Z_{10\%}$) and 1% ($Z_{1\%}$) of irradiance for the 1-m depth bin. We calculated $Z_{1\%}$ and $Z_{10\%}$, by linearly interpolating $\zeta(z, \lambda_{tag})$ between the depth bins that were immediately above and below the target optical depths. To allow for a qualitative evaluation of the extent of the bottom nepheloid layer, we also used $K_d(z, \lambda_{tag})$ to calculate a nepheloid layer index (NLI), which we define as:

$$NLIz = 100 * \left(\frac{K_d(z_{bot}, \lambda_{tagz} - \overline{K_d(z, \lambda_{tag})}}{\overline{K_d(z, \lambda_{tag})}z} \right) z \qquad (6$$

where $K_d(z_{bot}, \lambda_{tag})$ is the mean $K_d(z, \lambda_{tag})$ for the bottom five meters of a cast and $\overline{K_d(z, \lambda_{tag})}$ is the mean for the entire cast.

3.1.3 CTD data processing

From 2008 to 2017, temperature, salinity, and depth data were collected using a CTD (Falmouth Scientific Instruments NXIC CTD or Teledyne RD Instruments Citadel CTD-NV). CTDs sampled at a rate of 15 Hz. CTD data from each cast were binned to 1-m resolution and used to derive profiles of temperature (°C), salinity (PSS-78), and density anomaly, σ_t (kg m^{-3}) (Cokelet, 2016). For each profile, we calculated mixed layer depth (MLD) as the shallowest depth where the density anomaly first exceeded the average value from the upper 5 m by 0.1 kg m^{-3} and bottom layer depth (BLD) as the deepest depth where the density anomaly first exceeded the average value from the bottom 5 m by 0.1 kg m^{-3} (Cokelet, 2016; Danielson et al., 2011). If the density anomaly did not exceed the threshold, we did not calculate a bottom layer depth, and considered the mixed layer depth to be equal to the bottom depth. We also calculated the density difference between the mixed layer and bottom layer, $\Delta\sigma_t$, which we defined as the difference between σ_t average for the upper 5 m of the water column and the density at either 30 m below the mixed layer depth, or the deepest measurement in the water column (Cokelet, 2016).

3.2 Analysis

3.2.1 Satellite validation

We evaluated whether $K_d(z, \lambda_{tag})$ were reliable (accurate and precise) by comparing data from $K_d(z, \lambda_{tag})$ profiles to the European Space Agency's (ESA) Ocean Colour Climate Change Initiative (OC-CCI Version 5.0) daily, 4-km resolution downwelling diffuse attenuation coefficients at 490 nm, $K_d(z_s, 490)$ where z_s is the near-surface portion of the water column that is 'visible' to the satellite. OC-CCI $K_d(z_s, 490)$ is a multi-sensor satellite data product (NASA, NOAA, ESA, Copernicus) that is derived from inherent optical properties calculated using the Quasi-Analytical Algorithm (Lee et al., 2002; Lee et al., 2005). For our evaluation, we found all same-day spatial match-ups between OC-CCI $K_d(z_s, 490)$ and the final $K_d(z, \lambda_{tag})$ profiles. We first excluded upcast profiles to avoid pseudoreplication in our evaluation. We also excluded downcasts where $E_d(1, \lambda_{tag})$ was estimated by the algorithm. We followed Zaneveld et al. (2005) to calculate surface-weighted values of $K_d(z_s, \lambda_{tag})$ from the remaining $K_d(z, \lambda_{tag})$ profiles.

To evaluate the reliability of the tag-based data products, we fit a linear regression model between $\log_{10}$-transformed $K_d(z_s, \lambda_{tag})$ (predictor) and $\log_{10}$-transformed satellite $K_d(z_s, 490)$ (response), then used the model to calculate four performance metrics : the coefficient of determination (r^2), root mean square log error (RMSLE),

$$\text{RMSLE}z = N^{-1z}\sum_{i=1z}^{Nz}\sqrt{\left(\ln K_d(\widehat{z_s, 4}90z_i - \ln K_d(z_s, 490z_i)\right)^2}\,,z \qquad (7z$$

mean relative error (MRE),

$$\mathrm{MRE} = \frac{100}{N}\sum_{i=1}^{N}\frac{\left|\widehat{K_d(z_s,490)}_i - K_d(z_s,490)_i\right|}{K_d(z_s,490)_i}, \qquad (8)$$

and mean absolute error (MAE),

$$\mathrm{MAE} = 10^{\left(N^{-1}\sum_{i=1}^{N}\left|\log_{10}\widehat{K_d(z_s,490)}_i - \log_{10}K_d(z_s,490)_i\right|\right)}. \qquad (9)$$

We consider RMSLE, MRE, and MAE to be more informative than r^2 because they are less sensitive to outliers and the dynamic range of samples in the data set (Seegers et al., 2018).

We used relative error from the regression to evaluate whether there were detectable biases caused by obtaining measurements across a broad range of solar zenith angles (30°–90°). Solar zenith angle can cause 5–30% variation in K_d near the surface depending on wavelength and optical properties of active constituents in the water column because measurements are influenced by the angular distribution of the radiance field (Baker and Smith, 1979; Kirk, 2011).

3.2.2 Regional analysis

We conducted analyses at regional and fine spatial scales to evaluate whether regional patterns and trends were representative of finer-scale variability and vice versa, and to generate hypotheses about mechanisms responsible for variation in AOPs. For the regional analyses, we characterized region-wide patterns and trends in AOPs and associations between AOPs and physical covariates.

Because depth has often been used as a proxy for ambient irradiance in visual ecology, we evaluated whether depth was a reasonable predictor of subsurface irradiance in the eastern Bering Sea. To do so, we fit a generalized additive model (GAM) between maximum sampling depth for a cast, z_{max} (predictor), and near-bottom optical depth, $\zeta(z_{max})$ (response) and calculated the deviance explained by the model. We focused on bottom depth because it is most relevant to environmental conditions for highly abundant bottom-dwelling species in the eastern Bering Sea.

We tested for regional temporal trends in $\zeta(z_{max}, \lambda_{tag})$, $Z_{10\%}$, and $Z_{1\%}$ using linear-mixed effects models where $\zeta(z_{max}, \lambda_{tag})$, $Z_{10\%}$, and $Z_{1\%}$ were response variables, year was a continuous fixed effect, and survey station was a random effect. Because observations from a single haul are not independent samples, we weighted casts in the models by the number of casts from a station in a single year that passed quality control checks.

To evaluate if region-wide variation in the level of near-bottom radiation was explained by variation in near-surface water clarity and if water clarity was related to physical covariates (mixed layer depth, $\Delta\sigma_t$), we performed linear regressions on indices of $\zeta(z_{max}, \lambda_{tag})$, $Z_{10\%}$, $Z_{1\%}$, mixed layer depth, and $\Delta\sigma_t$. The indices were calculated from the annual interpolated raster surfaces (Supplementary Material: *Spatial interpolation to generate rasters*) as:

$$I_t = N^{-1z} \sum_{k=1z}^{Nz} \frac{(\hat{y}_{itz} - \hat{\mu}_{iz}}{\hat{s}_i}, z \qquad (4$$

where N is the number of 5 km x 5 km pixels in the interpolated surface (17,765), I_t is the anomaly index for year t, $\hat{y}_{itz}$ is the estimated value of $\zeta(z_{max}, \lambda_{tag})$, $Z_{10\%}$, or $Z_{1\%}$ for pixel i, $\hat{\mu}_{iz}$ is the mean for the pixel, and $\hat{s}_i$ is the standard deviation for the pixel. This approach was used to calculate anomalies instead of directly using observations because data were missing from different combinations of stations each year. We then fit linear regression models between combinations of anomaly indices to evaluate whether shelf-wide variation in near-bottom irradiance was explained by variation in near-surface water clarity (*i.e.*, $Z_{10\%}$, $Z_{1\%}$), whether variation in near-surface water clarity and near-bottom irradiance were explained by variation in physical covariates (mixed layer depth, $\Delta\sigma_t$), and whether there was covariation between physical covariates.

3.2.3 Fine-scale analysis

For the fine-scale analysis, we characterized patterns and trends using interpolated 5 × 5 km resolution raster surfaces of environmental variables ($\zeta(z_{max}, \lambda_{tag})$, $Z_{10\%}$, $Z_{1\%}$, mixed layer depth, $\Delta\sigma_t$), interpolated transects of environmental variables (Rows C, G, P, S; Fig. 1), and vertical profiles from individual stations. We analyzed fine-scale areal patterns in $\zeta(z_{max}, \lambda_{tag})$, $Z_{10\%}$, $Z_{1\%}$, mixed layer depth, and the nepheloid layer index by calculating pixel-wise summary statistics from annual raster surfaces. To evaluate whether the density structure of the water column was related to fine-scale variation in irradiance and water clarity (indirectly through processes that affect optically active constituents), we conducted regressions between annual raster surfaces of $\zeta(z_{max}, \lambda_{tag})$, $Z_{10\%}$, $Z_{1\%}$, mixed layer depth, and $\Delta\sigma_t$. We analyzed fine-scale vertical patterns by visually inspecting cross-sections of $K_d(z, \lambda_{tag})$, mixed layer depth, $Z_{10\%}$ and $Z_{1\%}$ that were interpolated along survey rows.

To test for fine-scale temporal trends, we conducted pixel-wise linear regressions on annual rasters of $\zeta(z_{max}, \lambda_{tag})$, $Z_{10\%}$, $Z_{1\%}$, using year as a predictor. In an effort to identify potential causes of change, we then examined vertical profiles of $K_d(z, \lambda_{tag})$ from areas where the slope of the relationship was significantly different from zero at the $p < 0.05$ level, based on a *t*-test.

3.2.4 Comparison with Bering10K ROMS model

We compared AOP patterns to predicted patterns of chlorophyll and detritus from a coupled bio-physical regional ocean model (Bering10K-BESTNPZ) in order to qualitatively validate our AOPs and evaluate whether patterns of $K_d(z, \lambda_{tag})$ were associated with predicted patterns of chlorophyll and detritus. Our regional ocean model uses the Regional Ocean Modeling System (ROMS), a free-surface, primitive equation hydrographic model (Haidvogel et al., 2008; Shchepetkin and McWilliams, 2005). The Bering Sea implementation, referred to as the Bering10K domain, spans the Bering Sea and northern Gulf of Alaska with 10-km horizontal resolution and 30 terrain-following depth levels. The physical model is coupled to the Bering Ecosystem Study nutrient-phytoplankton-zooplankton (BESTNPZ) biogeochemical model, which simulates lower trophic level dynamics spanning the pelagic, benthic, and ice environments (Gibson and Spitz, 2011; Kearney et al., 2020).

In this analysis, we use output from the hindcast simulation of the Bering10K-BESTNPZ model. The hindcast simulation covers the period of 1970 to the present, using surface and lateral boundary forcing from the Climate Forecast System Reanalysis (CFSR) (Saha et al., 2010; 1995–March 2011) and the Climate Forecast System Operational Analysis (CFSv2-OA) (April 2011–present). Further details of this model configuration, as well as analysis of the simulation's biophysical skill, can be found in Kearney et al. (2020). For this study, we examine simulated chlorophyll-a across the two phytoplankton size classes (large and small), as well as the concentration of detrital matter in the water column, to elucidate possible mechanisms influencing the observed patterns in $K_d(z, \lambda_{tag})$.

4. RESULTS

4.1 Satellite analysis

Performance metrics from the regression between $K_d(z_s, \lambda_{tag})$ and OC-CCI $K_d(z_s, 490)$ demonstrate that our data collection method and algorithm provide a reliable measure of near-surface K_d based on the strong positive correlation and 23.3% mean relative error (Fig. 3A; Table 1). There were no clear spatial patterns in prediction error, based on a visual inspection of relative error (Fig. 3B). Contrary to expectation, we did not detect a systematic bias in measurements due to solar zenith angles (32°–90°), based on residuals from the linear regression model (Fig. S7).

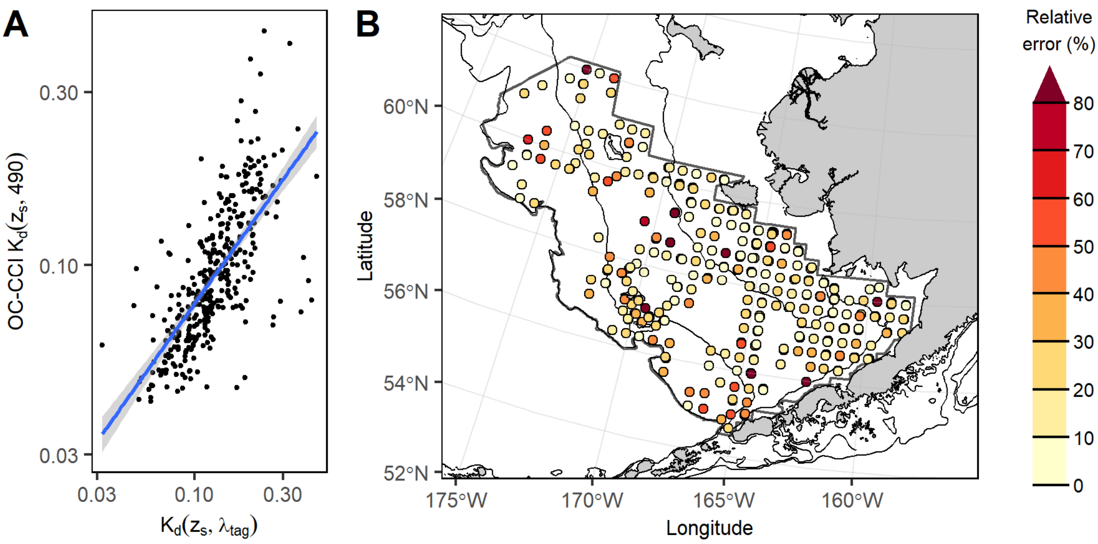

Figure 3. Surface-weighted archival tag $K_d(z_s, \lambda_{tag})$ versus OC-CCI $K_d(z_s, 490)$. (A) Linear regression model fit between log10-transformed $K_d(z_s, \lambda_{tag})$ and log-transformed OC-CCI $K_d(z_s, 490)$, shown by the solid blue line and shaded area (mean ± 2 standard errors); (B) Relative error (%) of regression fit over space, based on an absolute scale. See Table 1 for regression performance metrics.

Table 1. Performance metrics and slope for the regression between archival tag $K_d(z_s, \lambda_{tag})$ and OC-CCI $K_d(z_s,$ 490). Performance metrics are the coefficient of determination (r^2), mean relative error (MRE), root mean square log

error (RMSLE), and mean absolute error (MAE). Also shown are the fitted mean regression slopes and sample sizes (n).

Metric	Value
r^2	0.49
MRE (%)	23.3
RMSLE	0.227
MAE	1.254
Slope	0.72
n	351

4.2 Regional and fine-scale analyses

4.2.1 Regional patterns and trends

At a regional scale, depth was not a reliable predictor of near-bottom downwelling irradiance, as the GAM between z_{max} and $\zeta(z_{max}, \lambda_{tag})$ explained only 53.0% of total deviance (Fig. 4). There was a positive relationship between z_{max} and $\zeta(z_{max}, \lambda_{tag})$ at depths <80 m. The relationship was relatively flat at depths ≥ 80 m, which suggests bottom depth was not a reliable predictor of irradiance at these depths. There was considerable interannual variation in $\zeta(z_{max}, \lambda_{tag})$ as shown by the range of $\zeta(z_{max}, \lambda_{tag})$ at individual stations during 2004–2018 (Fig. 4). Ranges of $\zeta(z_{max}, \lambda_{tag})$ between 2004–2018 were 2.57–12.72 (median: 5.52), corresponding with 1.1–5.5 (median: 2.4) orders of magnitude of variation in near-bottom downwelling irradiance at individual stations (Fig. 4). From 2004 to 2018, 22.1% of stations (83/376) had variation in $\zeta(z_{max}, \lambda_{tag})$ corresponding with greater than three orders of magnitude of variation in near-bottom downelling irradiance (range of $\zeta(z_{max}, \lambda_{tag})$ > 6.9).

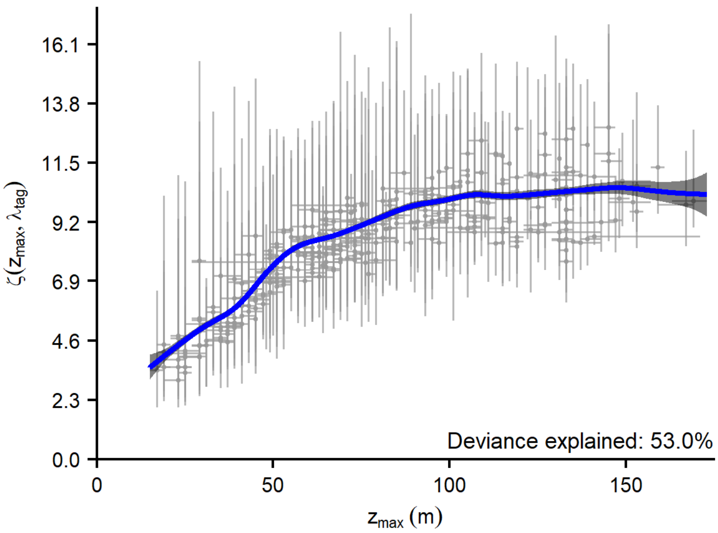

Figure 4. Maximum profile depth (z_{max}, λ_{tag}) versus near-bottom optical depth $\zeta(z_{max},$, $\lambda_{tag})$ from 2004–2018. Points denote station median, vertical and horizontal bars denote the range. Generalized additive model fit shown by solid blue line and shaded area (mean ± 2 std. err.). GAM deviance explained: 53.0%.

Lower near-surface water clarity was associated with a darker near-bottom environment as shown by the strong negative correlation between the $Z_{10\%}$ and $\zeta(z_{max}, \lambda_{tag})$ anomalies during 2004–2018 ($r_{[15]}$ = -0.79; p = 0.00042; Fig. 5A). A deeper mixed layer was also associated with weaker stratification, as shown by the strong negative correlation between mixed layer depth and density difference anomalies during 2008–2017 ($r_{[10]}$ = -0.81; p = 0.0044; Fig 5B). However, there was no evidence that variation in near-surface water clarity was linked to variation in the density structure of the water column, as density anomalies were not correlated with $Z_{10\%}$ anomalies ($r_{[10]}$ = 0.09; p = 0.80; Fig. 5C) or near-bottom optical depth anomalies ($r_{[10]}$ = -0.32; p = 0.37), and mixed layer depth anomalies were not correlated with $Z_{10\%}$ anomalies ($r_{[10]}$ = -0.10; p = 0.78) or near-bottom optical depth anomalies ($r_{[10]}$ = 0.03; p = 0.94).

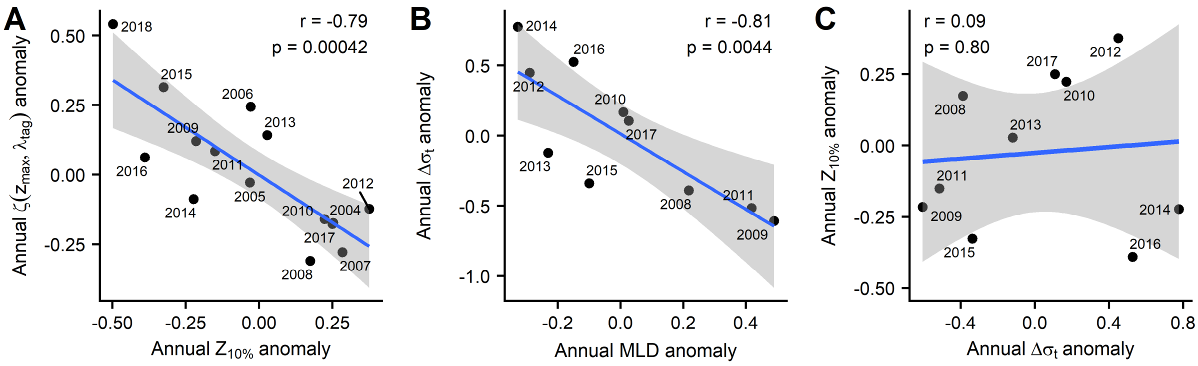

Figure 5. Relationships between anomaly indices for (A) $Z_{10\%}$ versus $\zeta(z_{max}, \lambda_{tag})$ from 2004–2018, (B) mixed layer depth versus $\Delta\sigma_t$ from 2008–2017, (C) $\Delta\sigma_t$ versus $Z_{10\%}$ from 2008–2017. Solid blue line and shading denote the linear regression fitted-mean ± two standard errors. The Pearson correlation coefficient (r) and p-value are shown on each panel.

Near-surface water clarity decreased and the near-bottom environment grew darker from 2004–2018, based on the effect of year in the linear mixed effects models (Table 2). On average, $\zeta(z_{max}, \lambda_{tag})$ increased by 0.035 ± 0.008 yr^{-1} (mean ± 2 std. err.), $Z_{10\%}$ decreased by 0.14 ± 0.03 m yr^{-1}, and $Z_{1\%}$ decreased by 0.21 ± 0.05 m yr^{-1}.

Table 2. Estimated slopes (mean ± 2 standard errors) of linear mixed effects models between year (predictor) and $Z_{10\%}$, $Z_{1\%}$, and $\zeta(z_{max}, \lambda_{tag})$, where stations were included as a random effect.

Response	Slope ($year^{-1}$)
$Z_{10\%}$	-0.14 ± 0.03
$Z_{1\%}$	-0.21 ± 0.05
$\zeta(z_{max}, \lambda_{tag})$	0.035 ± 0.008

4.2.2 Fine-scale patterns and trends

The reason why depth alone was not a reliable predictor of near-bottom optical depth (Fig. 4) is illustrated by spatial patterns in near-bottom optical depth (Fig. 6A). Although $\zeta(z_{max}, \lambda_{tag})$ generally increased with depth, near-bottom conditions were darker inshore of the continental shelf break in the north and in the middle domain in the southeast, as shown by areas of high average $\zeta(z_{max}, \lambda_{tag})$ during 2004–2018 (Fig. 6A). Over the northwest middle and outer shelf, near-surface water clarity was high as shown by the 25–30 m deep $Z_{10\%}$ (Fig. 6B), but near-bottom conditions were dark, as shown by the high $\zeta(z_{max}, \lambda_{tag})$. In part, this can be explained by a near-bottom nepheloid layer in the northwest (Fig. 6C). However, the nepheloid layer alone did not explain the disconnect between $Z_{10\%}$ and $\zeta(z_{max}, \lambda_{tag})$ in the northwest, as will be shown later.

In the northern middle and outer domain, $Z_{10\%}$ was deeper than the mixed layer depth during 2008–2017 due to high near-surface water clarity and a shallow mixed layer (Figs. 6E). This is notable because the mixed layer of the eastern Bering Sea is nutrient-depleted after the spring bloom and onset of stratification, but nutrient concentrations below the mixed layer over the middle and outer domain are sufficient to sustain primary production during summer if there is sufficient light (Mordy et al., 2012; Stabeno et al., 2012a). By contrast, $Z_{10\%}$ was shallower than the mixed layer over the southern middle and outer domain (Figs. 6E). In the inner domain, $Z_{10\%}$ was shallower than the mixed layer of the typically fully mixed water column. The inner domain is nutrient-depleted after the spring bloom, however, so light is not expected to be the limiting factor for primary production (Kachel et al., 2002; Mordy et al., 2017).

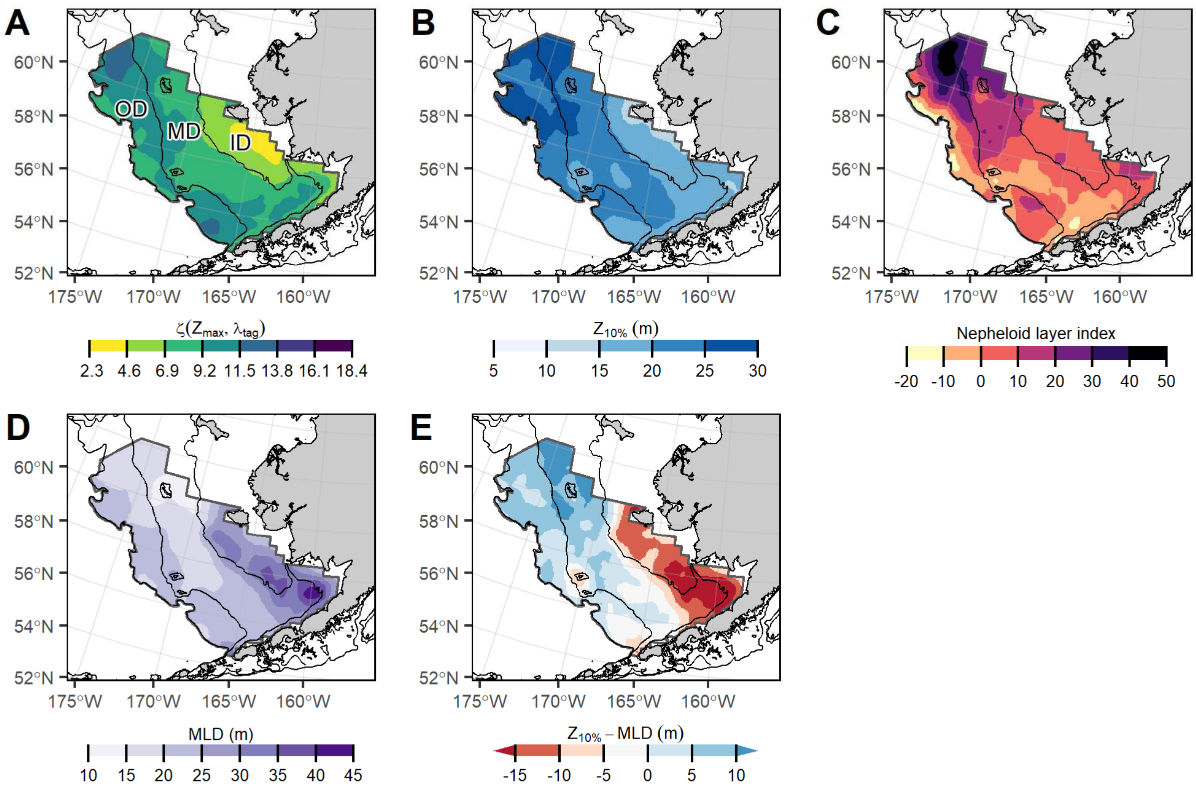

Figure 6. Means of (A) near-bottom optical depth, $\zeta(z_{max}, \lambda_{tag})$, for 2004–2018, (B) depth of the 10% irradiance, $Z_{10\%}$, for 2004–2018, (C) nepheloid layer index (NLI) for 2004–2018, (D) mixed layer depth for 2008–2017, (E) depth of $Z_{10\%}$ minus mixed layer depth for 2008–2017. Text labels in panel A denote the Inner (ID), Middle (MD), and Outer (OD) domains.

Measures of near-surface water clarity, $Z_{10\%}$ and $Z_{1\%}$, were strongly correlated over most of the eastern Bering Sea shelf during 2004–2018 (Fig. 7A). However, over the northern middle and outer domains, $Z_{10\%}$ and $Z_{1\%}$ were weakly correlated or uncorrelated and $Z_{10\%}$ and $\zeta(z_{max}, \lambda_{tag})$ were uncorrelated, indicating that near-surface water clarity was not the primary driver of variation in subsurface light (Fig. 7B). Further south and in the inner domain, $Z_{10\%}$ was strongly correlated with $\zeta(z_{max}, \lambda_{tag})$, indicating that variation in near-surface water clarity was closely linked to variation in light transmission through the full water column (Fig. 7B).

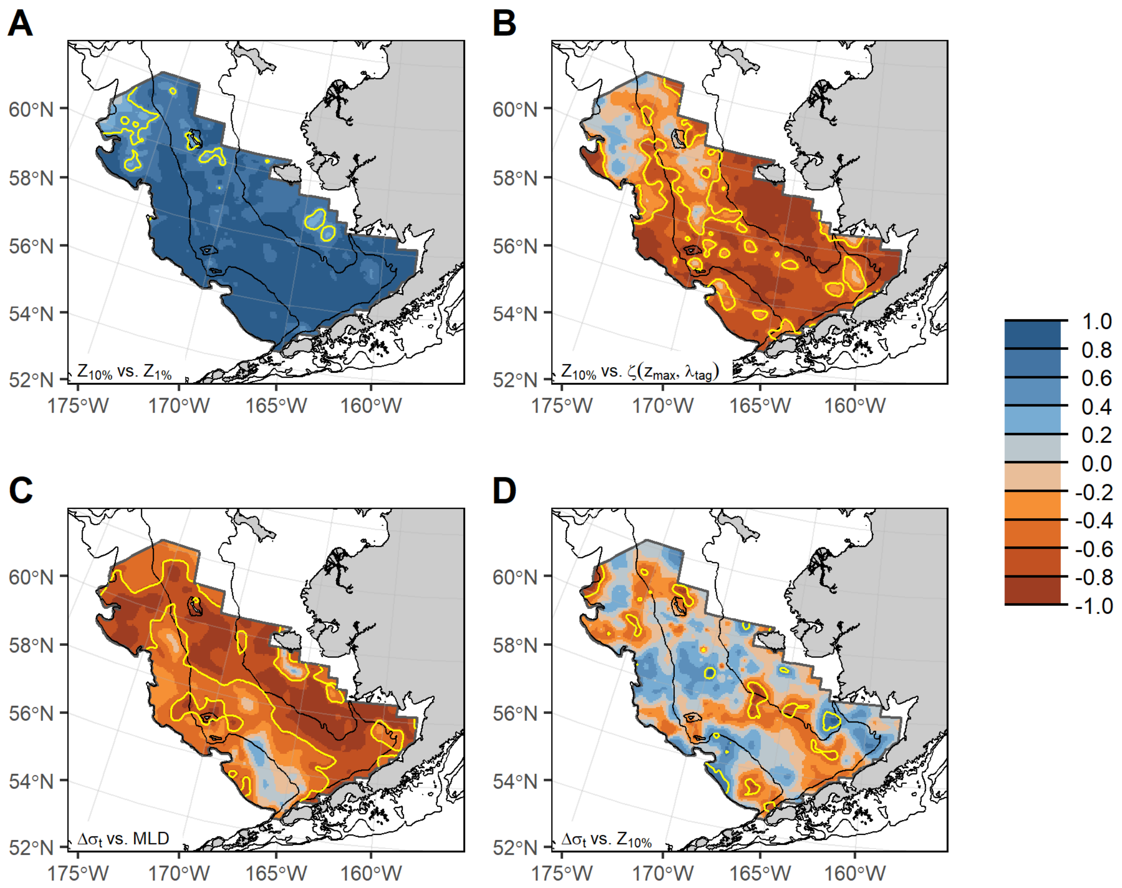

Figure 7. Pearson correlation coefficients (r) for (A) $Z_{10\%}$ versus $Z_{1\%}$ for 2004–2018; (B) $Z_{10\%}$ versus $\zeta(z_{max}, \lambda_{tag})$ for 2004–2018; (C) $\Delta\sigma_t$ versus mixed-layer depth for 2007–2017; (D) $\Delta\sigma_t$ versus $Z_{10\%}$ for 2007–2017. Yellow contour lines denote the areas with a non-zero correlation at the α = 0.05 significance level.

In the north (>~58° N), bottom and midwater light attenuating layers played an important role in regulating light transmission to the seafloor. This is shown by profiles of $K_d(z, \lambda_{tag})$ along rows P and S during 2011 (Figs. 8A,E) and 2017 (Figs. 8B,F). The thickness of the pycnocline decreased towards the inner domain as bottom depth decreased. In the northern middle and outer domain, mixed layer depth was often shallower than $Z_{10\%}$ and there was a recurrent mid-water peak in $K_d(z, \lambda_{tag})$ associated with the pycnocline or bottom of the mixed layer. Mid-water peaks in $K_d(z, \lambda_{tag})$ were likely caused by a subsurface chlorophyll maximum. In the bottom layer of the outer and middle domain, $K_d(z, \lambda_{tag})$was elevated in a 15–50 m thick bottom-associated nepheloid layer. Together, midwater and bottom layers caused dark near-bottom conditions in the middle and outer domain of the northwest (Fig. 6A) despite low $K_d(z, \lambda_{tag})$ in the mixed layer.

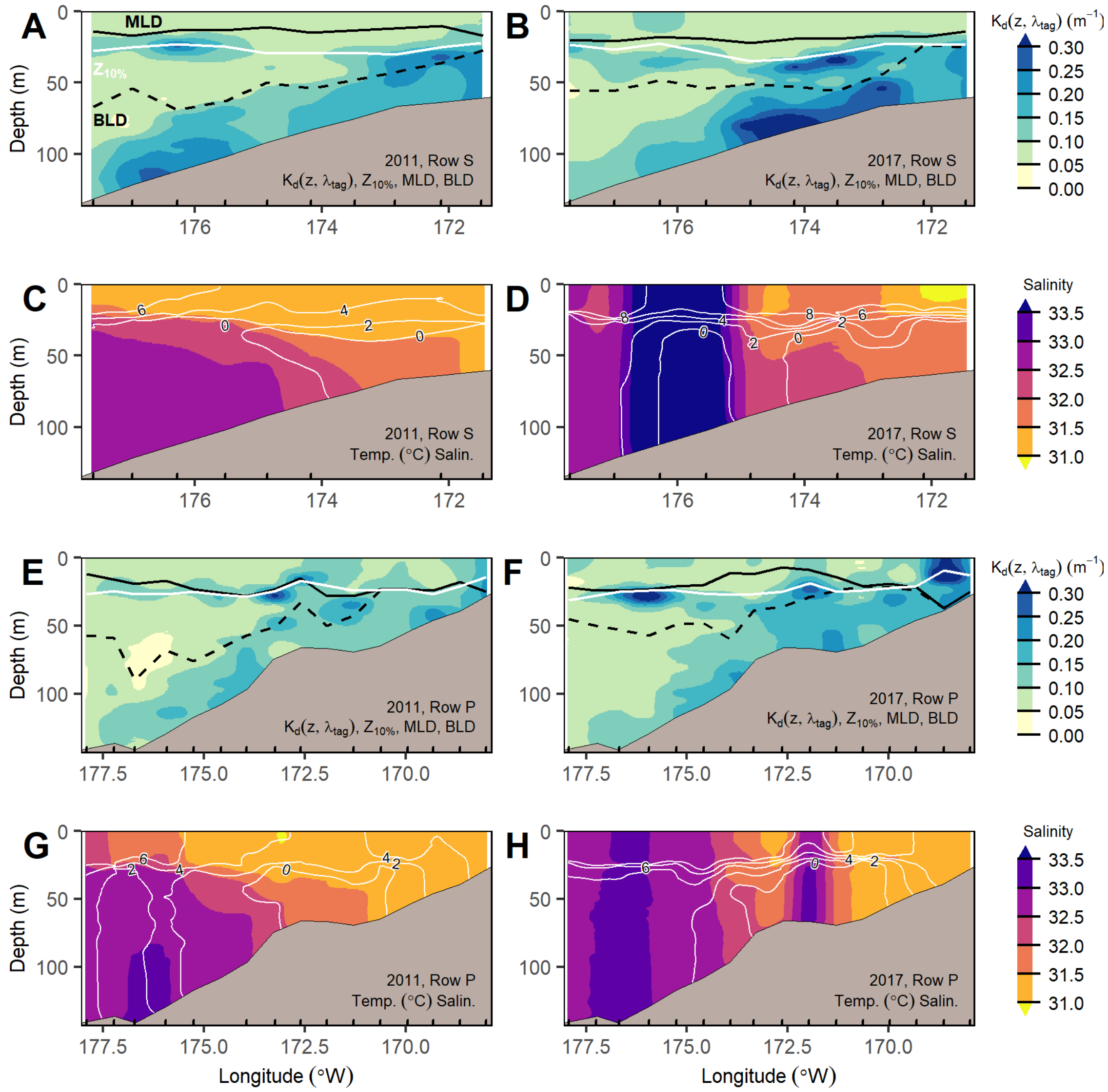

Figure 8. Cross-shelf profiles of optical and physical variables for rows S and P during 2011 and 2017. Panels show: (A, B, E, F) the vertical attenuation coefficient (color), mixed layer depth (MLD; solid black line), bottom layer depth (BLD; dashed black line), $Z_{10\%}$ (solid white line); (C, D, G, H) salinity (color) and temperature (white lines). Ticks along the horizontal axis denote sample locations for optical and physical variables that were obtained using

archival tags and CTDs, respectively. Row S was sampled from 7/18–7/21 in 2011 and 7/23–7/30 in 2017; row P was sampled from 7/3–7/23 in 2011 and 6/30–7/29 in 2017.

Vertical profiles of $K_d(z, \lambda_{tag})$ were more variable in the south, as shown by profiles along rows C and G during 2011 and 2017 (Figs. 9A, B, E, F). Over the middle domain, the vertical structure in $K_d(z, \lambda_{tag})$ was characterized by fine-scale (≤ 20 nmi) variability during many years, and near-surface water clarity played an important role in regulating light transmission, as shown by the row G cross-section during 2011 (Fig. 9A). Unlike in the north, there was no consistent bottom-associated nepheloid layer over the middle and outer domain in the south. Patches of elevated near-bottom $K_d(z, \lambda_{tag})$ values occurred sporadically, such as along row C at ~165.0 °W in 2011 (Fig. 9E) and at ~166.5 °W and 164.0 °W in 2017 (Fig. 9F). Due to variations in near-surface water clarity and mixed layer depth, the position of $Z_{10\%}$ relative to mixed layer depth was highly variable in the south, as shown by $Z_{10\%}$ being shallower than the mixed layer over the middle domain of row G during 2011 and much deeper during 2017 (Fig. 9A, B). Over the southern middle domain, there was often a sharp pycnocline between the mixed layer and bottom layer and, in contrast to the north, there was no regular peak in $K_d(z, \lambda_{tag})$ associated with the pycnocline—midwater peaks in $K_d(z, \lambda_{tag})$ only occurred sporadically. However, a sharp pycnocline was not always present in the south, potentially because the pycnocline was still forming in early summer (e.g. Fig. 9G).

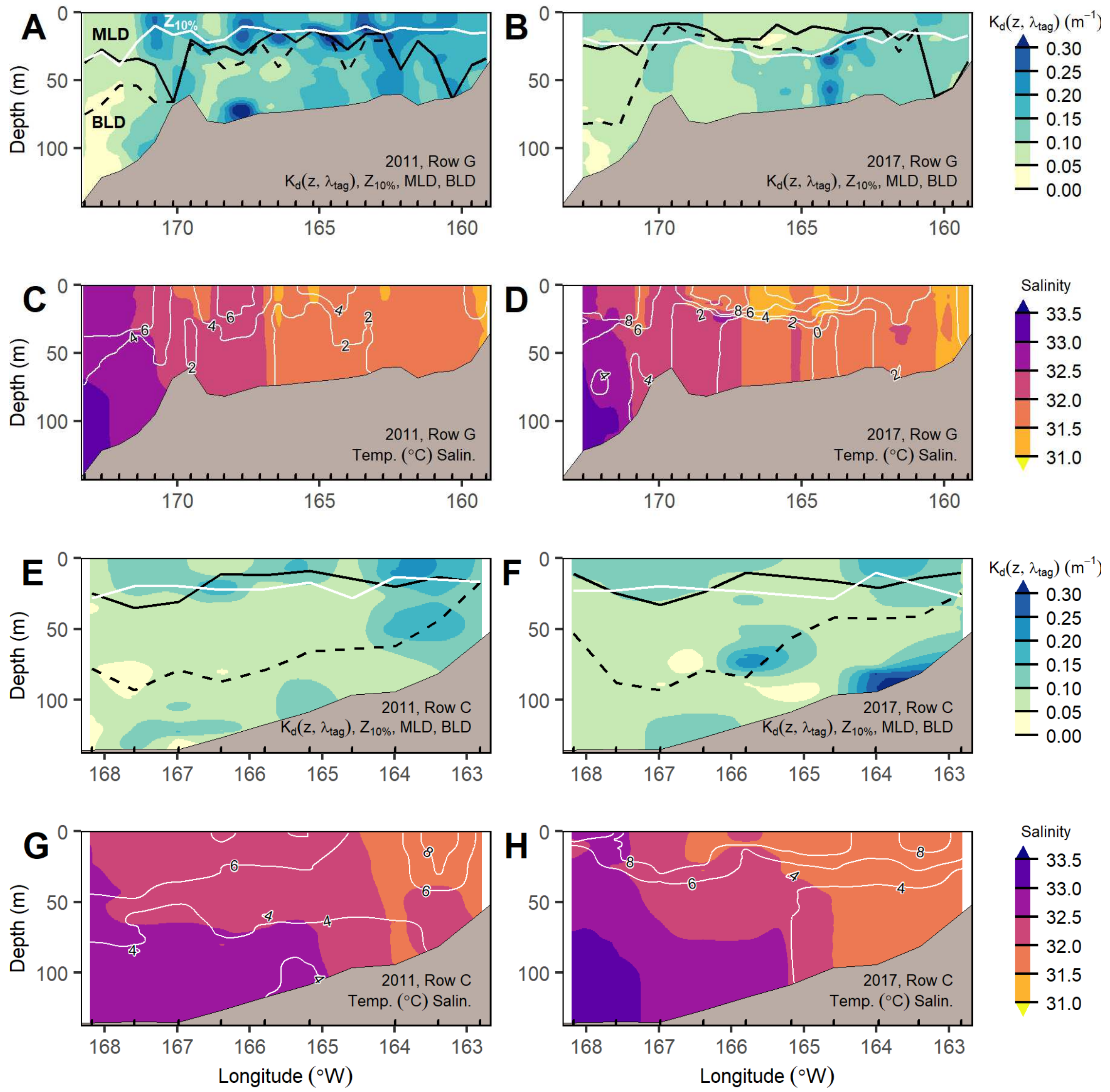

Figure 9. Cross-shelf profiles of optical and physical water column structure for rows G and C during 2011 and 2017. Panels show: (A, B, E, F) the vertical attenuation coefficient (color), mixed layer depth (MLD; solid black line), bottom layer depth (BLD; dashed black line), $Z_{10\%}$ (solid white line); (C, D, G, H,) salinity (color) and temperature (white lines). Ticks along the horizontal axis denote sample locations for optical and physical variables that were obtained using archival tags and CTDs, respectively. Row C was sampled from 6/10–7/14 in 2011 and 6/10–7/1 in 2017; row G was sampled from 6/5–7/15 in 2011 and 6/4–7/18 in 2017.

Trends in $\zeta(z_{max}, \lambda_{tag})$, $Z_{10\%}$, and $Z_{1\%}$ were patchy at fine-spatial scales and, in some areas, were the opposite of the regional trends of increasing $\zeta(z_{max}, \lambda_{tag})$ and decreasing $Z_{10\%}$, and $Z_{1\%}$

during 2004–2018 (Figs. 10A–C). Decreasing $Z_{10\%}$ was most prominent along the 50 m isobath north of 57 °N, in the interior of Bristol Bay, and inshore of the 50 m isobath south of Nunivak Island (Fig. 10A). Decreasing $Z_{1\%}$ occurred over the middle shelf and outer shelf in areas centered at ~58 °N and along the 50 m isobaths in Bristol Bay. Increases in $\zeta(z_{max}, \lambda_{tag})$ occurred in the same areas as the decreases in $Z_{1\%}$, while a significant decrease in $\zeta(z_{max}, \lambda_{tag})$ occurred over the northern outer shelf at ~ 61 °N (Fig. 10C).

In areas where there were significant changes in $\zeta(z_{max}, \lambda_{tag})$, $Z_{10\%}$, and $Z_{1\%}$, cumulative moving averages of $K_d(z, \lambda_{tag})$ at representative stations provide insight into how changes in the vertical structure of $K_d(z, \lambda_{tag})$ drove temporal trends. In the area around station K-03 (58° 18' N, 166° 33' W), a general increase in $K_d(z, \lambda_{tag})$ throughout the water column (Fig. 10D) led to the decrease in $Z_{10\%}$ and $Z_{1\%}$ and an increase in $\zeta(z_{max}, \lambda_{tag})$, although the trend was not monotonic (Figs. 10A–C). In the area around station I-25 (57° 40' N, 172° 48' W), an increase in $K_d(z, \lambda_{tag})$ near the surface and bottom (Fig. 10D) led to a decrease in $Z_{10\%}$ and $Z_{1\%}$ and an increase in $\zeta(z_{max}, \lambda_{tag})$ (Figs. 10A–C). Around Station S-30 (61° 00' N, 176° 58'W), a decrease in $K_d(z, \lambda_{tag})$ at depths >40 m (Fig. 10D) led to a decrease in $\zeta(z_{max}, \lambda_{tag})$ (Figs. 10A–C).

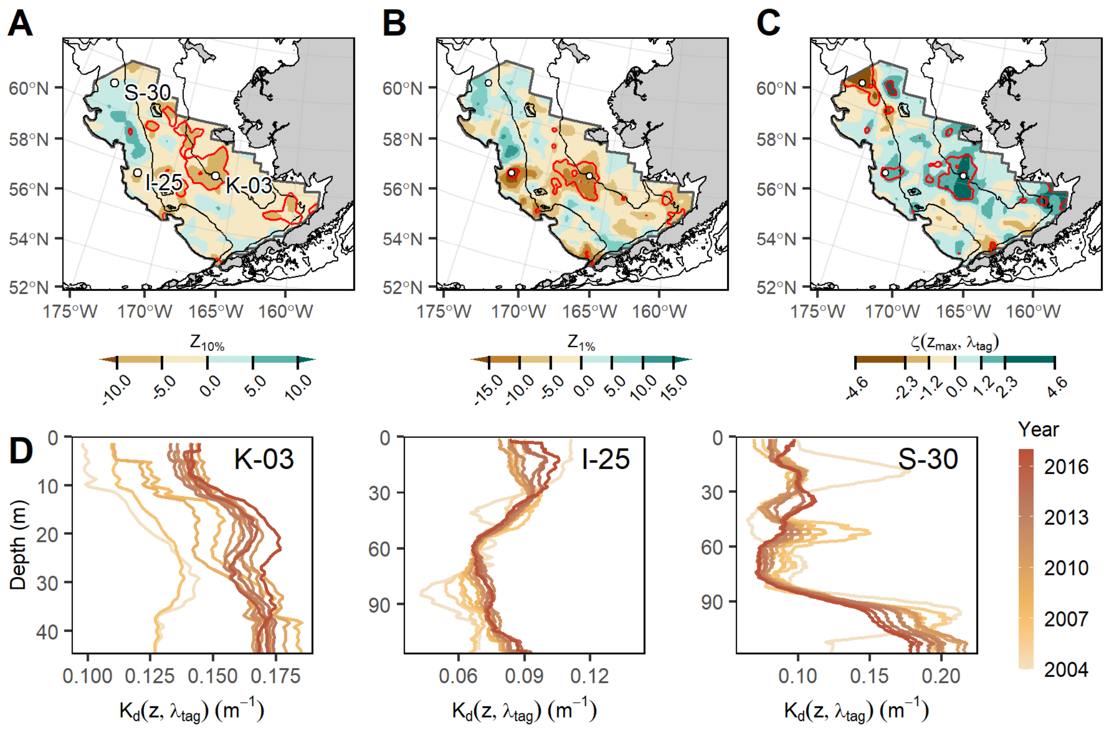

Figure 10. Total change in (A) $Z_{10\%}$, (B) $Z_{1\%}$, (C) $\zeta(Z_{max}, \lambda_{tag})$ between 2004 and 2018 based on the mean of pixel-wise linear regression on annual raster surfaces; red contours denote areas where the regression slope was non-zero at the $\alpha = 0.05$ level and points denote locations of stations for Panel D. Panel D shows the cumulative moving average of the vertical attenuation coefficient for stations K-03, I-25, and S-30 from 2004–2018, where line color denotes the year of the average.

4.3 Comparison with Bering10K model

The hypothesis that $K_d(z, \lambda_{tag})$ in the surface and mid-water was strongly influenced by variation in primary productivity is supported by predictions from the Bering10K-BESTNPZ model. Along rows C, G, P and S observed patterns in $K_d(z, \lambda_{tag})$ were qualitatively similar to modeled June–July chlorophyll-a for surface and mid-water depths (Figs. 8–9, 11). Throughout the eastern Bering Sea, model chlorophyll-a was higher during 2011 than 2017 (Figs 11, 12A–B), mainly due to effects of temperature on model dynamics. This pattern comports with observed differences in near-surface $K_d(z, \lambda_{tag})$ on the southern shelf between 2011 and 2017, as shown for rows C and G (Figs. 8–9). Further north, interannual variation in midwater $K_d(z, \lambda_{tag})$ was not clearly associated with modeled interannual variation chlorophyll-a (Figs. 8, 11). The model did not provide a mechanistic explanation for the bottom associated nepheloid layer, as chlorophyll-a and detritus were not elevated near the bottom over the middle and outer domain. The model predicted an onshore-offshore gradient in whole column detritus (Fig. 12C–D). Areal patterns of depth-integrated chlorophyll and detritus (Fig. 12) did not match the footprint of the bottom associated nepheloid layer (Fig. 6C).

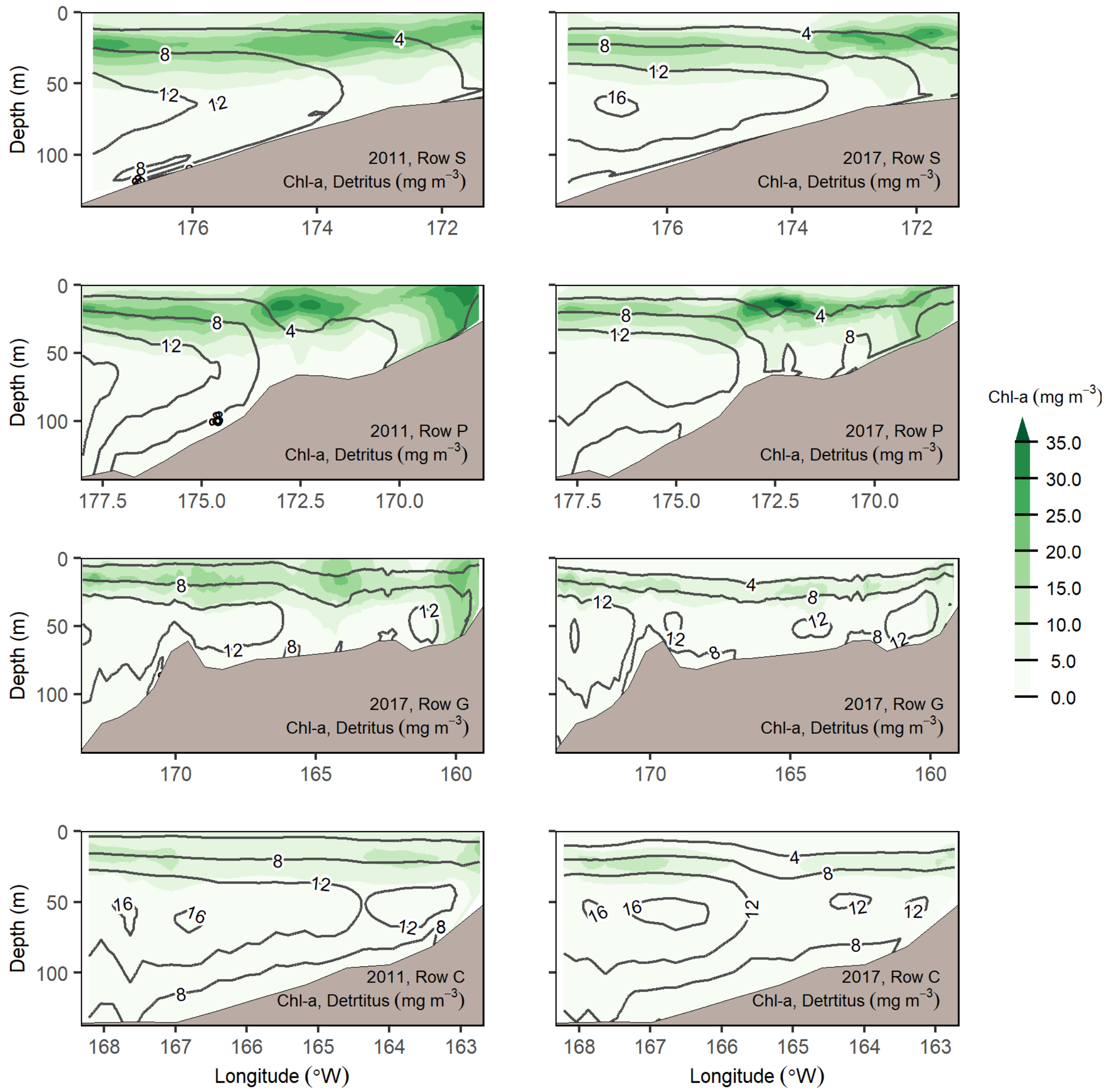

Figure 11. Modeled (Bering10K-BESTNPZ) concentrations of chlorophyll-a (mg m^{-3}) and detrital carbon (mg m^{-3}) along rows C, G, P, and S during June–July of 2011 and 2017. Fill color shows chlorophyll-a, contour lines show detrital carbon. Bottom depth follows trawl survey bathymetry rather than model bathymetry.

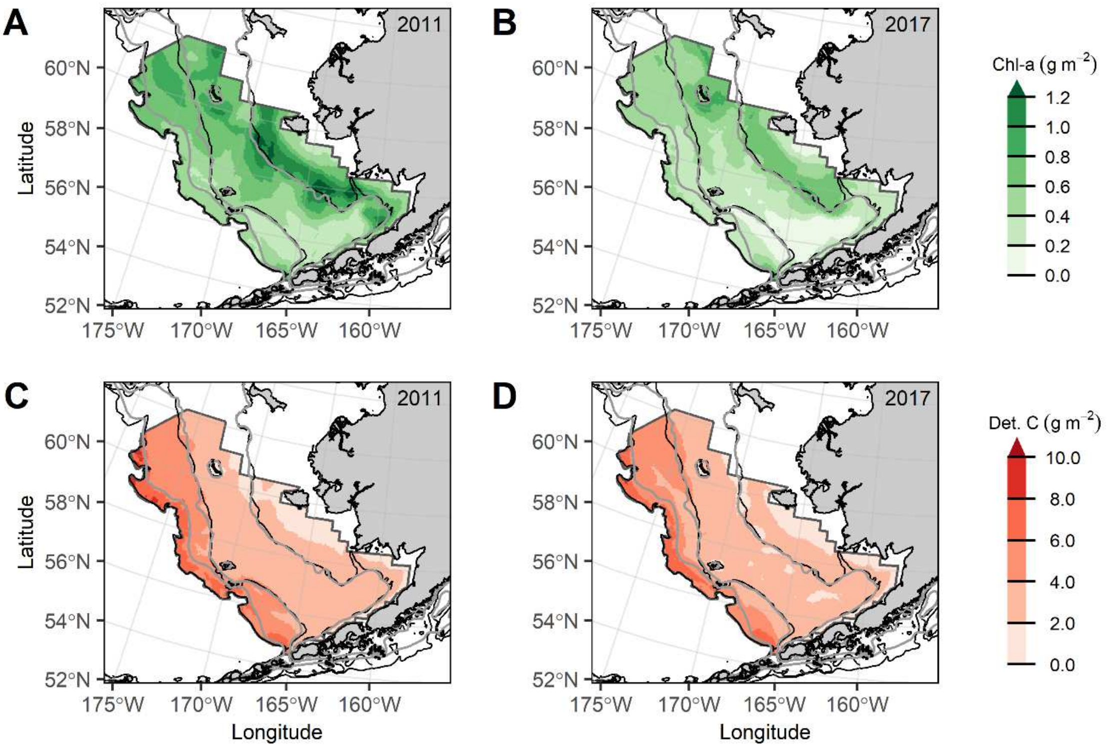

Figure 12. Modeled (Bering10K-BESTNPZ) depth-integrated chlorophyll-a (g m^{-2}) and detrital carbon (g m^{-2}) in the eastern Bering Sea during June–July 2011 and 2017. Black bathymetric contour lines show presumed survey bathymetry, grey lines show bathymetry used in the Bering10K-BESTNPZ model.

5. DISCUSSION

5.1 Overview

We characterized variation in subsurface water clarity in the eastern Bering Sea shelf at an unprecedented spatial resolution and annual frequency using AOPs derived from bottom trawl irradiance measurements. Based on performance metrics for the regression between archival tag $K_d(z_s, \lambda_{tag})$ and satellite $K_d(z_s, 490)$, we conclude the sampling method and algorithm provided a reliable characterization of in situ conditions. At a regional scale, we found the summertime near-bottom environment of the eastern Bering Sea grew darker and near-surface water clarity decreased from 2004 to 2018, as shown by the region-scale linear mixed effects models. Lower near-surface water clarity was associated with darker near-bottom conditions. At finer scales, however, local trends often differed from regional trends and changes in near-surface water clarity were not always associated with variation in irradiance deeper in the water column. These findings underscore that the eastern Bering Sea contains a complex mosaic of optical habitat and that subsurface dynamics play a key role in regulating optical conditions. Across the optical habitat mosaic, there are likely to be differences in primary productivity, trophic transfer efficiency, and community structure due to variation in light-dependent processes such as photosynthesis and visual foraging.

5.2 Patterns and trends

Over the northern middle and outer shelf, the recurrent peak in attenuation around the pycnocline was likely caused by a subsurface chlorophyll maximum, as predicted by the Bering10K-BESTNPZ model and frequently observed by in situ sampling (Stabeno et al., 2012b). Over the northern middle and outer shelf, high near-surface water clarity allows light to penetrate through the mixed layer and into the nutrient-rich waters below, where primary production can continue throughout the summer (Mordy et al., 2012; Stabeno et al., 2012a, 2012b). However, substances other than chlorophyll-a may also affect light transmission through the pycnocline, as concentrations of non-algal particulate and CDOM can be higher in subsurface layers than in the mixed layer (Naik et al., 2013).

Although patterns of $K_d(z, \lambda_{tag})$ generally matched spatial patterns of total chlorophyll predicted by the Bering10K-BESTNPZ model in the surface and midwater, they did not match modeled interannual variation in subsurface total chlorophyll in the north and the model did not provide a mechanistic explanation for the bottom-associated nepheloid layer. The mismatch between observed $K_d(z, \lambda_{tag})$ and modeled patterns of interannual variation in subsurface chlorophyll-a in the northern region may derive from the BESTNPZ model's inability to fully simulate the under-ice and ice-edge phytoplankton blooms and sinking dynamics that occur in this region (Kearney et al., 2020). The absence of a nepheloid layer may be due to the fact that the Bering10K-BESTNPZ model does not include sediment resuspension dynamics. It may also point to model deficiencies related to sinking, remineralization, and resuspension of organic matter in this region. Overall, dynamics of the Bering10K-BESTNPZ model are poorly constrained by in-situ observations due to a paucity of observations, especially with respect to spatial variation in the north. The tag-based AOP data set or future trawl-based AOP data may help to improve the Bering10K-BESTNPZ model by informing efforts to constrain or refine processes in the model.

We hypothesize that the bottom-associated nepheloid layer over the northern middle and outer shelf is maintained by tidally-driven resuspension of sediment. Nepheloid layers form when current velocities along the seafloor generate enough shear stress to resuspend substrate. The shear stress needed to resuspend sediment depends on the composition of the sediment. Flow velocities ≥7 cm s^{-1} generate enough shear stress to resuspend phytodetrital aggregates (Lampitt, 1985; McCave, 2019), 10–15 cm s^{-1} can resuspend loosely consolidated silt, and 25–30 cm s^{-1} can resuspend sand (Gardner, 1989). Mean geostrophic flow velocities are < 5 cm s^{-1} over most of the eastern Bering Sea shelf (Cokelet, 2016; Stabeno et al., 2016), insufficient to resuspend sediment. However, diurnal and semidiurnal tides in the eastern Bering Sea generate 10–30 cm s^{-1} currents over much of the shelf and currents >70 cm s^{-1} can occur in some areas (Coachman, 1986; Stabeno et al., 2008). These current speeds would be sufficient to resuspend phytoplankton, detritus, and the predominantly mud and sand substrate of the eastern Bering Sea shelf, although tidal currents are weaker further north (Stabeno et al., 2012b). If it is caused by tidal currents, variation in the nepheloid layer would be caused by variation in accumulated phytoplankton and detritus in the bottom layer, tidal amplitude, composition of surface sediment, and rates of consumption by benthic consumers (Lampitt, 1985). Further research is needed to clarify what causes the nepheloid layer, what effect the nepheloid layer has on ecological processes near the seafloor, and why the nepheloid layer is most prominent in the north.

Contact between trawl gear and the seafloor generates sediment clouds, but is unlikely to explain the bottom-associated nepheloid layer for several reasons. First, review of hundreds of hours of underwater video footage of the 83-112 bottom-trawl gear in motion in the eastern Bering Sea shows the archival tag location (top panel, 0.5–1 m behind headrope, ~2.5 m off-bottom) is well outside of the mudcloud (L.L. Britt and S. Kotwicki, personal observation). Second, the nepheloid layer typically extends tens of meters off bottom, well beyond where a mud cloud would likely begin. Third, the grain size of seafloor sediment generally decreases from onshore-to-offshore on the eastern Bering Sea shelf (Richwine et al. 2018), which suggests mudclouds would be more prevalent in deeper areas. However, the nepheloid layer is absent or less pronounced in deep areas and patterns of sediment size (Richwine et al. 2018) do not align with the footprint of nepheloid layer. Thus, the nepheloid layer is unlikely to be an artifact of our sampling method.

5.3 Implications for fisheries stock assessment and management

The level of variation in near-bottom optical depth is likely sufficient to cause variation in the catchability (*i.e.*, capture efficiency) of bottom trawl surveys. At many survey stations, variation in $\zeta(z_{max}, \lambda_{tag})$ corresponded with multiple-order-of magnitude variation in downwelling irradiance that would be expected to cause variation in capture efficiency. A 3–4 order-of-magnitude decrease in background irradiance can cause a complete cessation of fish visual reactions to bottom trawl gear (Blaxter and Parrish, 1966, 1964; Cui et al., 1991; Glass and Wardle, 1989) and variation in downwelling irradiance during bottom trawl surveys affects catch rates of walleye pollock in the eastern Bering Sea (Kotwicki et al., 2018, 2009). Changes in catchability can be a concern for fisheries management because they affect the precision and accuracy of fisheries indices of abundance that are used for stock assessment (Wilberg et al., 2009). The relatively low cost of the archival tags and minimal disruption to bottom trawl survey operations suggests that archival tags could similarly be deployed on commercial fishing gear to improve understanding of how variation in light and water clarity affects catchability.

Similarly, variation in near-bottom optical depth may also affect demographic rates of fish populations by altering the strength of predator-prey interactions (Eiane et al., 1999). As with trawl efficiency, the ability of a fish to feed visually can cease entirely given a 2–4 order-of-magnitude change in background irradiance (*e.g.* Ryer et al., 2002; Utne, 1997). The effect of a change in water clarity on predator-prey interactions depends on the visual capabilities of the predator and prey, the relative visibility of prey, and foraging mode of predators (*e.g.* Eiane et al., 1999; Giske et al., 1994; Rohan et al., In review). Reduced water clarity affects piscivory more than planktivory (De Robertis et al., 2003), and favors tactile feeding over visual feeding (Eiane et al., 1999).

Depth is often treated as a proxy for the ambient level of radiation in visual ecology studies and species distribution models (Caves et al., 2017; Kaartvedt et al., 2017, 1996; Schweikert et al., 2018) but it is not a reliable predictor of optical depth in the eastern Bering

Sea. Studies in the eastern Bering Sea may benefit from using optical depth to characterize the level of ambient radiation, such as by using it as a predictor in species distribution models. Doing so may clarify how visual habitat requirements influence fish distribution and habitat availability in the eastern Bering Sea.

Changes in water clarity can indicate changes in the dynamics of primary production and thereby productivity of higher trophic levels. The trend of decreasing near-bottom optical depth over the northern middle-outer domain indicates there has been a decrease in optically active substances (*i.e.*, chlorophyll-a, CDOM, non-algal particulate) in the water column during the survey period. The trend is notable because it occurred in an area where primary productivity continues throughout the summer by virtue of high near-surface water clarity, high nutrient availability below the mixed layer, and a gradual pycnocline (Stabeno et al., 2012a). The reason for this change may be the decline in dissolved inorganic nitrate and phosphate in the bottom layer that occurred from summer 2005 to 2016 that would presumably affect primary production and chlorophyll in the pycnocline (Stabeno et al., 2019). The change from 2005–2016 was associated with a concomitant decrease in salinity, indicating nutrient variability was mediated by physical processes (Stabeno et al., 2019). Alternative explanations could be changes in the timing of productivity or shifts in the balance between primary production and consumption. Further research is needed to evaluate whether changes in optical depth were associated with changes in salinity productivity, which may be facilitated by developing empirical models that relate $K_d(z, \lambda_{tag})$ to chlorophyll-a concentrations (e.g. Bayle et al., 2015; O'Toole et al., 2014).

5.4 Limitations and uncertainties

Our sampling method and analyses have several limitations and uncertainties when it comes to characterizing changes in water clarity in the eastern Bering Sea. First, we treated year as the time step for our analyses, but surveys were sampled over two months every year, progressing from interior Bristol Bay to the northwest outer continental shelf. Because individual stations were sampled at approximately the same time each year, the optical properties provide an annual snapshot of the system. However, sampling within-year, between years, and among stations was conducted at different times relative to the non-stationary phenology of phytoplankton blooms, stratification, sea-ice retreat, and tides. Second, the archival tags do not collect spectral irradiance measurements so we could not derive spectrally-resolved AOPs. This is an important limitation because photopigments of autotrophs and animals are sensitive to specific colors of light, and the different substances that cause variation in the optical environment have spectral differences in absorption and scattering. Third, we could not verify what caused variation in AOPs because we did not conduct any sampling to determine how the composition of optically-active constituents of the water column changed over space and time. Instead, our inferences are based on previous work to elucidate how physical and biological processes affect water clarity in the eastern Bering Sea. Finally, the wide acceptance angle of the archival tag photodiode suggests archival tag measurements can approximate, but are not equal to diffuse irradiance because tags are not equipped with a cosine corrector. While we do not believe these issues meaningfully affected our results and interpretation, improving sampling methods or constraining analyses to particular subsets of the data can overcome some of these limitations and uncertainties. Moreover, the patterns we identified may be useful for guiding focused process-oriented research using more sophisticated sampling methods and instrumentation.

5.5 Methodological improvements

Our sampling method could be modified to improve characterization of visual conditions for animals and identification of optically active constituents of the water column. We used archival tags equipped with photodiodes because they have a large range of absolute sensitivity and could withstand the rough operating conditions of bottom trawl surveys with little risk of equipment failure. This required a trade-off in terms of information quality and comparability with measurements from conventional sampling equipment. In the future, archival tags could be replaced with purpose-built optical sampling equipment if the equipment meets the operational requirements for bottom trawl surveys (*e.g.* ruggedized, low profile to minimize drag on the trawl). Bio-optical sampling equipment could be deployed alongside archival tags to develop models that characterize relationships between physical constituents of the water column and tag-derived AOPs in the eastern Bering Sea, as has been done using archival tags deployed on marine animals (Bayle et al., 2015; Jaud et al., 2012; O'Toole et al., 2014; Teo et al., 2009). Spectral radiometers could be deployed to derive spectrally specific AOPs or archival tags could be equipped with spectral filters that match wavelengths that are relevant to vision or other biological processes (*e.g.* Gal et al., 1999). All of these options represent cost-efficient solutions to improve in situ monitoring.

5.6 Conclusions

Monitoring subsurface water clarity in marine ecosystems remains an immense logistical challenge. While burgeoning technologies such as autonomous underwater vehicles, biogeochemical Argo floats, and satellite-based high spectral resolution LiDAR may eventually achieve broader coverage and improve subsurface monitoring, coverage gaps will persist in the near-term. In the meantime, researchers should continue to explore how existing sampling platforms can be used to fill coverage gaps. Our study provides one such method for monitoring subsurface water clarity.

ACKNOWLEDGMENTS

We thank the survey participants who collected data for this study, including the masters and crews of FV *Alaska Knight*, FV *Aldebaran*, FV *Arcturus*, FV *Ocean Explorer*, and FV *Vesteraalen*. We thank Cal Mordy, Jens Nielsen, Steve Rubin, Jeff Napp, Morgan Arrington, Cheryl Barnes, Tim Essington, Helena McMonagle, and two anonymous reviewers for constructive feedback on an earlier version of this manuscript. Funding to support this research was provided by the NOAA Fisheries and the Environment (FATE) Program and the Joint Institute for the Study of the Atmosphere and Ocean (JISAO) under NOAA Cooperative Agreement NA15OAR4320063. This manuscript is contribution number EcoFOCI-0953 to NOAA PMEL-AFSC's Ecosystems and Fisheries-Oceanography Coordinated Investigations, contribution number 5143 to NOAA's Pacific Marine Environmental Laboratory, and contribution 2020-1101 to JISAO. Any use of trade, firm, or product names is for descriptive purposes only and does not imply endorsement by the U.S. Government. The scientific results and conclusions, as well as any views or opinions expressed herein, are those of the author(s) and do not necessarily reflect those of NOAA or the Department of Commerce.

AUTHOR CONTRIBUTIONS

Conceptualization: SR, SK, KK, JS, DB, LB, SZ
Methodology: SR, SK, KK, JS, EL, EC, KA, SZ
Software: SR, SK, KK, JS, EL
Validation: SR, SK, KK, EL, EC
Formal analysis: SR, KK, JS
Investigation: SR, EL, EC, LB
Data curation: SR, SK, EL, EC, JS
Writing-Original: SR, KK, JS
Writing-Review & Editing: All authors
Visualization: SR, KK, JS
Project administration: SK, KA
Funding acquisition: SR, SK, DB, LB, KA, SZ
Supervision: SK, DB, LB, KA

REFERENCES

Aksnes, D.L., 2007. Evidence for visual constraints in large marine fish stocks. Limnol. Oceanogr. 52, 198–203. https://doi.org/10.4319/lo.2007.52.1.0198

Aksnes, D.L., Nejstgaard, J., Sædberg, E., Sørnes, T., 2004. Optical control of fish and zooplankton populations. Limnol. Oceanogr. 49, 233–238. https://doi.org/10.4319/lo.2004.49.1.0233

Aksnes, D.L., Ohman, M.D., 2009. Multi-decadal shoaling of the euphotic zone in the southern sector of the California Current System. Limnol. Oceanogr. 54, 1272–1281. https://doi.org/10.4319/lo.2009.54.4.1272

Baker, K.S., Smith, R.C., 1979. Quasi-inherent characteristics of the diffuse attenuation coefficient for irradiance. Ocean Opt. IV 208, 60–63.

Barbieux, M., Uitz, J., Gentili, B., Pasqueron De Fommervault, O., Mignot, A., Poteau, A., Schmechtig, C., Taillandier, V., Leymarie, E., Penkerc'H, C., D'Ortenzio, F., Claustre, H., Bricaud, A., 2019. Bio-optical characterization of subsurface chlorophyll maxima in the

Mediterranean Sea from a Biogeochemical-Argo float database. Biogeosciences 16, 1321–1342. https://doi.org/10.5194/bg-16-1321-2019

Bayle, S., Monestiez, P., Guinet, C., Nerini, D., 2015. Moving toward finer scales in oceanography: Predictive linear functional model of Chlorophyll *a* profile from light data. Prog. Oceanogr. 134, 221–231. https://doi.org/10.1016/j.pocean.2015.02.001

Bittig, H.C., Maurer, T.L., Plant, J.N., Wong, A.P., Schmechtig, C., Claustre, H., Trull, T.W., Bhaskar, T.V.S.U., Boss, E., Dall'Olmo, G., Organelli, E., Poteau, A., Johnson, K.S., Hanstein, C., Leymarie, E., Le Reste, S.L., Riser, S.C., Rupan, A.R., Taillandier, V., Thierry, V., Xing, X., 2019. A BGC-Argo guide: Planning, deployment, data handling and usage. Front. Mar. Sci. 6. https://doi.org/10.3389/fmars.2019.00502

Blaxter, J.H.S., Parrish, B.B., 1966. The reaction of marine fish to moving netting and other devices in tanks. Mar. Res. No. 1 1–15.

Blaxter, J.H.S., Parrish, B.B., 1964. The importance of vision in the reaction of fish to driftnets and trawls, in: Modern Fishing Gear of the World 2. Fishing News Books, London, pp. 529–536.

Boyce, D.G., Dowd, M., Lewis, M.R., Worm, B., 2014. Estimating global chlorophyll changes over the past century. Prog. Oceanogr. 122, 163–173. https://doi.org/10.1016/j.pocean.2014.01.004

Britt, L.L., Loew, E.R., McFarland, W.N., 2001. Visual pigments in the early life stages of Pacific Northwest marine fishes. J. Exp. Biol. 204, 2581–2587.

Brown, C.A., Huot, Y., Purcell, M.J., Cullen, J.J., Lewis, M.R., 2004. Mapping coastal optical and biogeochemical variability using an autonomous underwater vehicle and a new bio-optical inversion algorithm. Limnol. Oceanogr. Methods 2, 262–281.

https://doi.org/10.4319/lom.2004.2.262

Capuzzo, E., Stephens, D., Silva, T., Barry, J., Forster, R.M., 2015. Decrease in water clarity of the southern and central North Sea during the 20th century. Glob. Chang. Biol. 21, 2206–2214. https://doi.org/10.1111/gcb.12854

Caves, E.M., Sutton, T.T., Johnsen, S., 2017. Visual acuity in ray-finned fishes correlates with eye size and habitat. J. Exp. Biol. 220, 1586–1596. https://doi.org/10.1242/jeb.151183

Coachman, L.K., 1986. Circulation, water masses, and fluxes on the southeastern Bering Sea shelf. Cont. Shelf Res. 5, 23–108. https://doi.org/10.1016/0278-4343(86)90011-7

Cokelet, E.D., 2016. 3-D water properties and geostrophic circulation on the eastern Bering Sea shelf. Deep Sea Res. Part II Top. Stud. Oceanogr. 134, 65–85. https://doi.org/http://dx.doi.org/10.1016/j.dsr2.2016.08.009

Cui, G., Wardle, C.S., Glass, C.W., Johnstone, A.D.F., Mojsiewicz, W.R., 1991. Light level thresholds for visual reaction of mackerel, *Scomber scombrus* L., to coloured monofilament nylon gillnet materials. Fish. Res. 10, 255–263. https://doi.org/10.1016/0165-7836(91)90079-U

Cullen, J.J., 2015. Subsurface chlorophyll maximum layers: Enduring enigma or mystery solved? Ann. Rev. Mar. Sci. 7, 207–239. https://doi.org/10.1146/annurev-marine-010213-135111

Danielson, S., Eisner, L., Weingartner, T., Aagaard, K., 2011. Thermal and haline variability over the central Bering Sea shelf: Seasonal and interannual perspectives. Cont. Shelf Res. 31, 539–554. https://doi.org/10.1016/j.csr.2010.12.010

De Robertis, A., Ryer, C.H., Veloza, A., Brodeur, R.D., 2003. Differential effects of turbidity on prey consumption of piscivorous and planktivorous fish. Can. J. Fish. Aquat. Sci. 60, 1517–1526. https://doi.org/10.1139/f03-123

Dickman, E.M., Newell, J.M., González, M.J., Vanni, M.J., 2008. Light, nutrients, and food-chain length constrain planktonic energy transfer efficiency across multiple trophic levels. Proc. Natl. Acad. Sci. U. S. A. 105, 18408–18412. https://doi.org/10.1073/pnas.0805566105

Duntley, S.Q., 1963. Light in the sea. J. Opt. Soc. Am. 53, 214–233.

Dupont, N., Aksnes, D.L., 2013. Centennial changes in water clarity of the Baltic Sea and the North Sea. Estuar. Coast. Shelf Sci. 131, 282–289. https://doi.org/10.1016/j.ecss.2013.08.010

Eiane, K., Aksnes, D.L., Bagøien, E., Kaartvedt, S., 1999. Fish or jellies — a question of visibility? Limnol. Oceanogr. 44, 1352–1357. https://doi.org/10.4319/lo.1999.44.5.1352

Eiane, K., Aksnes, D.L., Giske, J., 1997. The significance of optical properties in competition among visual and tactile planktivores: a theoretical study. Ecol. Modell. 98, 123–136.

Feely, R.A., Massoth, G.J., Paulson, A.J., Lamb, M.F., Martin, E.A., 1981. Distribution and elemental composition of suspended matter in Alaskan coastal waters. NOAA Tech. Memo. ERL-PMEL-2, 119.

Gal, G., Loew, E.R., Rudstam, L.G., Mohammadian, A.M., 1999. Light and diel vertical migration: spectral sensitivity and light avoidance by *Mysis relicta*. Can. J. Fish. Aquat. Sci. 56, 311–322. https://doi.org/2

Gardner, W.D., 1989. Periodic resuspension in Baltimore Canyon by focusing of internal waves. J. Geophys. Res. 94. https://doi.org/10.1029/jc094ic12p18185

Gibson, G.A., Spitz, Y.H., 2011. Impacts of biological parameterization, initial conditions, and environmental forcing on parameter sensitivity and uncertainty in a marine ecosystem model for the Bering Sea. J. Mar. Syst. 88, 214–231. https://doi.org/10.1016/j.jmarsys.2011.04.008

Giske, J., Aksnes, D.L., Fiksen, Ø., 1994. Visual predators, environmental variables and zooplankton mortality risk. Vie Milieu 44, 1–9.

Glass, C.W., Wardle, C.S., 1989. Comparison of the reactions of fish to a trawl gear, at high and low light intensities. Fish. Res. 7, 249–266. https://doi.org/10.1016/0165-7836(89)90059-3

Gordon, H.R., 1989. Can the Lambert-Beer law be applied to the diffuse attenuation coefficient of ocean water? Limnol. Oceanogr. 34, 1389–1409. https://doi.org/10.1097/00003246-200206000-00018

Haidvogel, D.B., Arango, H., Budgell, W.P., Cornuelle, B.D., Curchitser, E., Di Lorenzo, E., Fennel, K., Geyer, W.R., Hermann, A.J., Lanerolle, L., Levin, J., McWilliams, J.C., Miller, A.J., Moore, A.M., Powell, T.M., Shchepetkin, A.F., Sherwood, C.R., Signell, R.P., Warner, J.C., Wilkin, J., 2008. Ocean forecasting in terrain-following coordinates: Formulation and skill assessment of the Regional Ocean Modeling System. J. Comput. Phys. 227, 3595–3624. https://doi.org/10.1016/j.jcp.2007.06.016

Harada, N., Sato, M., Oguri, K., Hagino, K., Okazaki, Y., Katsuki, K., Tsuji, Y., Shin, K.H., Tadai, O., Saitoh, S.I., Narita, H., Konno, S., Jordan, R.W., Shiraiwa, Y., Grebmeier, J., 2012. Enhancement of coccolithophorid blooms in the Bering Sea by recent environmental changes. Global Biogeochem. Cycles 26, 1–13. https://doi.org/10.1029/2011GB004177

Haraldsson, M., Tönnesson, K., Tiselius, P., Thingstad, T.F., Aksnes, D.L., 2012. Relationship between fish and jellyfish as a function of eutrophication and water clarity. Mar. Ecol. Prog. Ser. 471, 73–85. https://doi.org/10.3354/meps10036

Hemsley, V.S., Smyth, T.J., Martin, A.P., Frajka-Williams, E., Thompson, A.F., Damerell, G., Painter, S.C., 2015. Estimating oceanic primary production using vertical irradiance and chlorophyll profiles from ocean gliders in the North Atlantic. Environ. Sci. Technol. 49, 11612–11621. https://doi.org/10.1021/acs.est.5b00608

Hostetler, C.A., Behrenfeld, M.J., Hu, Y., Hair, J.W., Schulien, J.A., 2018. Spaceborne lidar in the study of marine systems. Ann. Rev. Mar. Sci. 10, 121–147. https://doi.org/10.1146/annurev-marine-121916-063335

Hunt, G.L., Coyle, K.O., Eisner, L., Farley, E. V, Heintz, R., Mueter, F., Napp, J.M., Overland, J.E., Ressler, P.H., Sale, S., Stabeno, P.J., 2011. Climate impacts on eastern Bering Sea food webs: A synthesis of new data and an assessment of the Oscillating Control Hypothesis. ICES J. Mar. Sci. 68, 1230–1243. https://doi.org/10.1093/icesjms/fsr036

Iida, T., Mizobata, K., Saitoh, S.I., 2012. Interannual variability of coccolithophore *Emiliania huxleyi* blooms in response to changes in water column stability in the eastern Bering Sea. Cont. Shelf Res. 34, 7–17. https://doi.org/10.1016/j.csr.2011.11.007

Jaud, T., Cile Dragon, A.-C., Garcia, J.V., Guinet, C., 2012. Relationship between chlorophyll a concentration, light attenuation and diving depth of the southern elephant seal *Mirounga leonina*. PLoS One 7, e47444. https://doi.org/10.1371/journal.pone.0047444

Jumars, P.A., Dorgan, K.M., Lindsay, S.M., 2015. Diet of worms emended: an update of polychaete feeding guilds. Ann. Rev. Mar. Sci. 7, 497–520. https://doi.org/10.1146/annurev-marine-010814-020007

Kaartvedt, S., Melle, W., Knutsen, T., Skjoldal, H.R., 1996. Vertical distribution of fish and krill beneath water of varying optical properties. Mar. Ecol. Prog. Ser. 136, 51–58. https://doi.org/10.3354/meps136051

Kaartvedt, S., Røstad, A., Aksnes, D.L., 2017. Changing weather causes behavioral responses in the lower mesopelagic. Mar. Ecol. Prog. Ser. 574, 259–263. https://doi.org/10.3354/meps07467

Kachel, N.B., Hunt, G.L., Salo, S.A., Schumacher, J.D., Stabeno, P.J., Whitledge, T.E., 2002. Characteristics and variability of the inner front of the southeastern Bering Sea. Deep. Res. Part II Top. Stud. Oceanogr. 49, 5889–5909. https://doi.org/10.1016/S0967-0645(02)00324-7

Kawana, K., 1975. Turbidity distribution of the Bering Sea in the summer. Bull. Fac. Fish. Hokkaido Univ. 26, 73–86.

Kearney, K., Hermann, A., Cheng, W., Ortiz, I., Aydin, K., 2020. A coupled pelagic-benthic-sympagic biogeochemical model for the Bering Sea: documentation and validation of the BESTNPZ model (v2019.08.23) within a high-resolution regional ocean model. Geosci. Model Dev. 13, 597–650. https://doi.org/10.5194/gmd-13-597-2020

Kirk, J.T.O., 2011. Light and photosynthesis in aquatic ecosystems, 3rd ed. Cambridge University Press, New York.

Kotwicki, S., De Robertis, A., von Szalay, P., Towler, R., 2009. The effect of light intensity on the availability of walleye pollock (*Theragra chalcogramma*) to bottom trawl and acoustic surveys. Can. J. Fish. Aquat. Sci. 66, 983–994. https://doi.org/10.1139/f09-055

Kotwicki, S., Ressler, P.H., Ianelli, J.N., Punt, A.E., Horne, J.K., 2018. Combining data from bottom trawl and acoustic surveys to estimate an index of abundance for semipelagic species. Can. J. Fish. Aquat. Sci. 75, 60–71.

Ladd, C., Eisner, L.B., Salo, S.A., Mordy, C.W., Iglesias-Rodriguez, M.D., 2018. Spatial and temporal variability of coccolithophore blooms in the eastern Bering Sea. J. Geophys. Res. Ocean. 123, 9119–9136. https://doi.org/10.1029/2018JC014302

Ladd, C., Stabeno, P.J., 2012. Stratification on the eastern Bering Sea shelf revisited. Deep Sea Res. Part II Top. Stud. Oceanogr. 65–70, 72–83. https://doi.org/10.1016/j.dsr2.2012.02.009

Laman, E.A., Kotwicki, S., Rooper, C.N., 2014. Correlating environmental and biogenic factors with abundance and distribution of Pacific ocean perch (*Sebastes alutus*) in the Aleutian Islands, Alaska. Fish. Bull. 113, 270–289. https://doi.org/10.7755/FB.113.3.4.The

Laman, E.A., Rooper, C.N., Turner, K., Rooney, S., Cooper, D.W., Zimmermann, M., 2018. Using species distribution models to describe essential fish habitat in Alaska. Can. J. Fish. Aquat. Sci. 75, 1230–1255. https://doi.org/10.1139/cjfas-2017-0181

Lampitt, R.S., 1985. Evidence for the seasonal deposition of detritus to the deep-sea floor and its subsequent resuspension. Deep Sea Res. Part A, Oceanogr. Res. Pap. 32, 885–897. https://doi.org/10.1016/0198-0149(85)90034-2

Langbehn, T.J., Varpe, Ø., 2017. Sea-ice loss boosts visual search: Fish foraging and changing pelagic interactions in polar oceans. Glob. Chang. Biol. 23, 5318–5330. https://doi.org/10.1111/gcb.13797

Lee, Z., Carder, K.L., Arnone, R.A., 2002. Deriving inherent optical properties from water color: a multiband quasi-analytical algorithm for optically deep waters. Appl. Opt. 41, 5755. https://doi.org/10.1364/ao.41.005755

Lee, Z.P., Du, K.P., Arnone, R., 2005. A model for the diffuse attenuation coefficient of downwelling irradiance. J. Geophys. Res. C Ocean. 110, 1–10. https://doi.org/10.1029/2004JC002275

Lomas, M., Eisner, L., Gann, J., Baer, S., Mordy, C., Stabeno, P., 2020. Time-series of direct primary production and phytoplankton biomass in the southeastern Bering Sea: Responses to cold and warm stanzas. Mar. Ecol. Prog. Ser. 642, 39–54. https://doi.org/10.3354/meps13317

Lovvorn, J.R., Baduini, C.L., Hunt Jr., G.L., 2001. Modeling underwater visual and filter feeding by planktivorous shearwaters in unusual sea conditions. Ecology 82, 2342–2356.

Lythgoe, J.., 1972. The adaptation of visual pigments to the photic environment, in: Dartnell, H.J.A. (Ed.), The Handbook of Sensory Physiology VII/1. Springer, pp. 566–603.

McCave, I.N., 2019. Nepheloid layers, 3rd ed, Encyclopedia of Ocean Sciences. Elsevier Ltd. https://doi.org/10.1016/B978-0-12-409548-9.11207-2

McManus, D.A., Smyth, C.S., 1970. Turbid bottom water on the continental shelf of the northern Bering Sea. J. Sediment. Petrol. 40, 869–873.

Mitchell, C., Gordon, H.R., Bowler, B., Drapeau, D., Balch, W.M., 2018. Optical inversions of the water column based on glider measurements. Opt. Express 26, 32824. https://doi.org/10.1364/oe.26.032824

Mobley, C.D., 1994. Light and water: Radiative transfer in natural waters. Academic Press.

Mordy, C.W., Cokelet, E.D., Ladd, C., Menzia, F.A., Proctor, P., Stabeno, P.J., Wisegarver, E., 2012. Net community production on the middle shelf of the eastern Bering Sea. Deep. Res. Part II Top. Stud. Oceanogr. 65–70, 110–125. https://doi.org/10.1016/j.dsr2.2012.02.012

Mordy, C.W., Devol, A., Eisner, L.B., Kachel, N., Ladd, C., Lomas, M.W., Proctor, P., Sambrotto, R.N., Shull, D.H., Stabeno, P.J., Wisegarver, E., 2017. Nutrient and phytoplankton dynamics on the inner shelf of the eastern Bering Sea. J. Geophys. Res. Ocean. 122, 2422–2440. https://doi.org/10.1002/2016JC012071

Naik, P., D’Sa, E.J., Gomes, H. do R., Goés, J.I., Mouw, C.B., 2013. Light absorption properties of southeastern Bering Sea waters: Analysis, parameterization and implications for remote sensing. Remote Sens. Environ. 134, 120–134. https://doi.org/10.1016/j.rse.2013.03.004

Nowak, B.V.R., 2019. In situ measurements by instrumented grey seals (*Halichoerus gryups*) reveal fine-scale oceanographic properties and environmental influences on movement patterns. Dalhouse University.

O'Toole, M., Guinet, C., Lea, M.A., Hindell, M.A., 2017. Marine predators and phytoplankton: How elephant seals use the recurrent Kerguelen plume. Mar. Ecol. Prog. Ser. 581, 215–227. https://doi.org/10.3354/meps12312

O'Toole, M.D., Lea, M.A., Guinet, C., Hindell, M.A., 2014. Estimating trans-seasonal variability in water column biomass for a highly migratory, deep diving predator. PLoS One 9. https://doi.org/10.1371/journal.pone.0113171

Olson, M.B., Strom, S.L., 2002. Phytoplankton growth, microzooplankton herbivory and community structure in the southeast Bering Sea: Insight into the formation and temporal persistence of an *Emiliania huxleyi* bloom. Deep. Res. Part II Top. Stud. Oceanogr. 49, 5969–5990. https://doi.org/10.1016/S0967-0645(02)00329-6

Opdal, A.F., Lindemann, C., Aksnes, D.L., 2019. Centennial decline in North Sea water clarity causes strong delay in phytoplankton bloom timing 3946–3953. https://doi.org/10.1111/gcb.14810

Pitarch, J., 2020. A review of Secchi's contribution to marine optics and the foundation of Secchi disk science. Oceanography 33, 26–37. https://doi.org/10.5670/oceanog.2020.301

Richwine, K.A., Smith, K.R., McConnaughey, R.A., 2018. Surficial sediments of the eastern Bering Sea continental shelf: EBSSED-2 database documentation. United States Department of Commerce, NOAA Technical Memorandum NMFS-AFSC-377, 48 p. https://doi.org/10.25923/yygp-xs96

Riisgård, H.U., Larsen, P.S., 2015. Filter-feeding zoobenthos and hydrodynamics, in: Rossi, S. (Ed.), Marine Animal Forests. Springer International Publishing, pp. 1–25.

https://doi.org/10.1007/978-3-319-17001-5

Rohan, S.K., Beauchamp, D.A., Essington, T.E., Hansen, A.G., *In review*. A generalized model of aquatic visual foraging.

Rohan, S.K., Kotwicki, S., Laman, E.A., Britt, L.L., Aydin, K., 2020. Deriving apparent optical properties from light measurements obtained using bottom-trawl-mounted archival tags. United States Department of Commerce, NOAA Technical Memorandum NMFS-AFSC-403, 91 p. https://doi.org/10.25923/42yn-1q79

Rooper, C.N., Hoff, G.R., Stevenson, D.E., Orr, J.W., Spies, I.B., 2019. Skate egg nursery habitat in the eastern Bering Sea: A predictive model. Mar. Ecol. Prog. Ser. 609, 163–178. https://doi.org/10.3354/meps12809

Ryer, C.H., Lawton, A., Lopez, R.J., Olla, B.L., 2002. A comparison of the functional ecology of visual vs. nonvisual foraging in two planktivorous marine fishes. Can. J. Fish. Aquat. Sci. 59, 1305–1314. https://doi.org/10.1139/f02-097

Sambrotto, R.N., Niebauer, H.J., Goering, J.J., Iverson, R.L., 1986. Relationships among vertical mixing, nitrate uptake, and phytoplankton growth during the spring bloom in the southeast Bering Sea middle shelf. Cont. Shelf Res. 5, 161–198. https://doi.org/10.1016/0278-4343(86)90014-2

Sandén, P., Håkansson, B., 1996. Long-term trends in Secchi depth in the Baltic Sea. Limnol. Oceanogr. 41, 346–351. https://doi.org/10.1016/j.ecss.2012.02.015

Sathyendranath, S., Brewin, R., Brockmann, C., Brotas, V., Calton, B., Chuprin, A., Cipollini, P., Couto, A., Dingle, J., Doerffer, R., Donlon, C., Dowell, M., Farman, A., Grant, M., Groom, S., Horseman, A., Jackson, T., Krasemann, H., Lavender, S., Martinez-Vicente, V., Mazeran, C., Mélin, F., Moore, T., Müller, D., Regner, P., Roy, S., Steele, C., Steinmetz, F., Swinton, J., Taberner, M., Thompson, A., Valente, A., Zühlke, M., Brando, V., Feng, H., Feldman, G., Franz, B., Frouin, R., Gould, R., Hooker, S., Kahru, M., Kratzer, S., Mitchell, B., Muller-Karger, F., Sosik, H., Voss, K., Werdell, J., Platt, T., 2019. An Ocean-Colour Time Series for Use in Climate Studies: The Experience of the Ocean-Colour Climate Change Initiative (OC-CCI). Sensors 19, 4285. https://doi.org/10.3390/s19194285

Schulien, J.A., Behrenfeld, M.J., Hair, J.W., Hostetler, C.A., Twardowski, M.S., 2017. Vertically- resolved phytoplankton carbon and net primary production from a high spectral resolution lidar. Opt. Express 25, 13577. https://doi.org/10.1364/oe.25.013577

Schweikert, L.E., Caves, E.M., Solie, S.E., Sutton, T.T., Johnsen, S., 2018. Variation in rod spectral sensitivity of fishes is best predicted by habitat and depth. J. Fish Biol. https://doi.org/10.1111/jfb.13859

Seegers, B.N., Stumpf, R.P., Schaeffer, B.A., Loftin, K.A., Werdell, P.J., 2018. Performance metrics for the assessment of satellite data products: an ocean color case study. Opt. Express 26, 7404. https://doi.org/10.1364/oe.26.007404

Shchepetkin, A.F., McWilliams, J.C., 2005. The regional oceanic modeling system (ROMS): A split-explicit, free-surface, topography-following-coordinate oceanic model. Ocean Model. 9, 347–404. https://doi.org/10.1016/j.ocemod.2004.08.002

Sigler, M.F., Stabeno, P.J., Eisner, L.B., Napp, J.M., Mueter, F.J., 2014. Spring and fall phytoplankton blooms in a productive subarctic ecosystem, the eastern Bering Sea, during 1995-2011. Deep. Res. Part II Top. Stud. Oceanogr. 109, 71–83. https://doi.org/10.1016/j.dsr2.2013.12.007

Smith, R.C., Baker, K.S., 1984. The analysis of ocean optical data, in: Blizard, M.A. (Ed.), SPIE, Ocean Optics VII. pp. 119–126. https://doi.org/10.1117/12.943295

Stabeno, P., Napp, J., Mordy, C., Whitledge, T., 2010. Factors influencing physical structure and lower trophic levels of the eastern Bering Sea shelf in 2005: Sea ice, tides and winds. Prog. Oceanogr. 85, 180–196. https://doi.org/10.1016/j.pocean.2010.02.010

Stabeno, P.J., Bell, S.W., 2019. Extreme conditions in the Bering Sea (2017–2018): record-breaking low sea-ice extent. Geophys. Res. Lett. 46, 8952–8959. https://doi.org/10.1029/2019GL083816

Stabeno, P.J., Bell, S.W., Bond, N.A., Kimmel, D.G., Mordy, C.W., Sullivan, M.E., 2019. Distributed Biological Observatory Region 1: Physics, chemistry and plankton in the northern Bering Sea. Deep. Res. Part II Top. Stud. Oceanogr. 162, 8–21. https://doi.org/10.1016/j.dsr2.2018.11.006

Stabeno, P.J., Danielson, S., Kachel, D., Kachel, N.B., Mordy, C.W., 2016. Currents and transport on the Eastern Bering Sea shelf: An integration of over 20 years of data. Deep Sea Res. Part II Top. Stud. Oceanogr. 134, 13–29. https://doi.org/10.1016/j.dsr2.2016.05.010

Stabeno, P.J., Duffy-Anderson, J.T., Eisner, L.B., Farley, E. V., Heintz, R.A., Mordy, C.W., 2017. Return of warm conditions in the southeastern Bering Sea: Physics to fluorescence. PLoS One 12, 1–16. https://doi.org/10.1371/journal.pone.0185464

Stabeno, P.J., Farley, E. V., Kachel, N.B., Moore, S., Mordy, C.W., Napp, J.M., Overland, J.E., Pinchuk, A.I., Sigler, M.F., 2012a. A comparison of the physics of the northern and southern shelves of the eastern Bering Sea and some implications for the ecosystem. Deep. Res. Part II Top. Stud. Oceanogr. 65–70, 14–30. https://doi.org/10.1016/j.dsr2.2012.02.019

Stabeno, P.J., Kachel, N., Mordy, C., Righi, D., Salo, S., 2008. An examination of the physical variability around the Pribilof Islands in 2004. Deep. Res. Part II Top. Stud. Oceanogr. 55, 1701–1716. https://doi.org/10.1016/j.dsr2.2008.03.006

Stabeno, P.J., Kachel, N.B., Moore, S.E., Napp, J.M., Sigler, M., Yamaguchi, A., Zerbini, A.N., 2012b. Comparison of warm and cold years on the southeastern Bering Sea shelf and some implications for the ecosystem. Deep. Res. Part II Top. Stud. Oceanogr. 65–70, 31–45. https://doi.org/10.1016/j.dsr2.2012.02.020

Stauffer, G., 2004. NOAA protocols for groundfish bottom-trawl surveys of the Nation's fishery resources. United States Department of Commerce, NOAA Technical Memorandum NMFS-F/SPO-65, 205 p.

Teo, S., Kudela, R., Rais, A., Perle, C., Costa, D., Block, B., 2009. Estimating chlorophyll profiles from electronic tags deployed on pelagic animals. Aquat. Biol. 5, 195–207. https://doi.org/10.3354/ab00152

Tolvanen, H., Suominen, T., Kalliola, R., 2013. Annual and long-term water transparency variations and the consequent seafloor illumination dynamics in the Baltic Sea archipelago coast of SW Finland. Boreal Environ. Res. 18, 446–458.

Utne, A., 1997. The effect of turbidity and illumination on the reaction distance and search time of the marine planktivore *Gobiusculus flavescens*. J. Fish Biol. 50, 926–938. https://doi.org/10.1111/j.1095-8649.1997.tb01619.x

Vacquié-Garcia, J., Mallefet, J., Bailleul, F., Picard, B., Guinet, C., 2017. Marine bioluminescence: measurement by a classical light sensor and related foraging behavior of a deep diving predator. Photochem. Photobiol. 93, 1312–1319. https://doi.org/10.1111/php.12776

Wernand, M.R., van der Woerd, H.J., Gieskes, W.W.C., 2013. Trends in ocean colour and chlorophyll concentration from 1889 to 2000, worldwide. PLoS One 8, e63766. https://doi.org/10.1371/journal.pone.0063766

Wilberg, M.J., Thorson, J.T., Linton, B.C., Berkson, J., 2009. Incorporating time-varying catchability into population dynamic stock assessment models. Rev. Fish. Sci. 18, 7–24. https://doi.org/10.1080/10641260903294647

Zaneveld, J.R. V., Barnard, A.H., Boss, E., 2005. Theoretical derivation of the depth average of remotely sensed optical parameters. Opt. Express 13, 9052–9061. https://doi.org/10.1364/opex.13.009052